Contact resonance atomic force microscopy using long elastic tips

To cite this article: Nadav Zimron-Politi and Ryan C Tung 2024 *Nanotechnology* **35** 075503

IOP Publishing Nanotechnology
Nanotechnology 35 (2024) 075503 (18pp) https://doi.org/10.1088/1361-6528/ad0bd2

Contact resonance atomic force microscopy using long elastic tips

Nadav Zimron-Politi and Ryan C Tung

Department of Mechanical Engineering, University of Nevada, Reno, 1664 N. Virginia St., Reno, NV 89557-0312, United States of America

E-mail: rtung@unr.edu

Received 22 September 2023, revised 20 October 2023
Accepted for publication 10 November 2023
Published 29 November 2023

Abstract

In this work, a new theoretical model for contact resonance atomic force microscopy, which incorporates the elastic dynamics of a long sensing tip is presented. The model is based on the Euler–Bernoulli beam theory and includes coupling effects from the two-beam structure, also known as an 'L-shaped' beam in the literature. Here, high-accuracy prediction of the sample stiffness, using several vibration modes with a relative error smaller than 10% for practical working ranges, is demonstrated. A discussion on the model's capability to predict the dynamic phenomena of eigenmode veering and crossing, as the force applied to the sample increases, is presented. The L-shaped beam model presented here is also applicable for structural applications such as: micro-electro-mechanical systems, energy harvesting, and unmanned aerial vehicle landing gear.

Keywords: contact resonance, atomic force microscopy, long elastic tip, qPlus sensor, nano-needle

1. Introduction

The atomic force microscope (AFM) traditionally uses a micro-cantilever beam to scan sample topography and measure sample material properties at the nano-scale. Contact resonance (CR) is a mode of AFM operation specifically designed for estimating mechanical properties while the AFM microcantilever tip is in the linear, net-repulsive region of the force-distance curve. The coupled sensor-sample natural frequencies, along with a theoretical model, are utilized for the estimation of the samples stiffness [1, 2]. Then, a contact mechanics model is used to relate the sample stiffness to the mechanical properties of the sample of interest. The application of CR in the linear region of the sensor-sample surface interaction force, allow scientists to model the sample stiffness using a linear spring, assuming small sample deformation. The AFM cantilever sensor is modeled using the Euler–Bernoulli beam theory, and the assumption of small amplitude vibrations. The combination of a simple beam model and simple sample model to describe a complicated physical phenomenon provides researchers with a powerful analytical tool for the analysis of nano-scale mechanical properties.

Scientists have employed the AFM to measure samples with a wide range of stiffnesses in various environments, including vacuum, air, and liquids, to accommodate the sample's specific requirements. However, when dealing with soft biological samples, new challenges emerge in both sensor design and data processing. In order for the biological samples to retain their original properties, measurements must be performed in the sample's native environment, i.e. a liquid environment. To enable *in situ* measurements of biological samples in their native environments, a new sensor design using a long sensing tip, sometimes referred to as a needle, has been introduced [3–10].

The use of a long sensing tip assures the micro-cantilever beam body is out of the liquid, thereby reducing hydrodynamic forces on the sensor body [11–15], and achieving a high-quality factor [8]. The described method, named trolling mode (TM), has been used to scan sample topography [8], take sample property measurements [7], and was used to demonstrate high-speed imaging of live biological samples [10]. The qPlus sensor uses a quartz tuning fork (QTF) with a tip attached to one of the tuning fork tines to perform force measurements with a pico-newton resolution [16, 17]. The qPlus sensor, in contrast to the micro-sensors commonly used in AFM, features a cantilevered beam that is an order of magnitude larger. This larger scale allows for more flexibility in design, fabrication, and attachment of the sensing tip. With

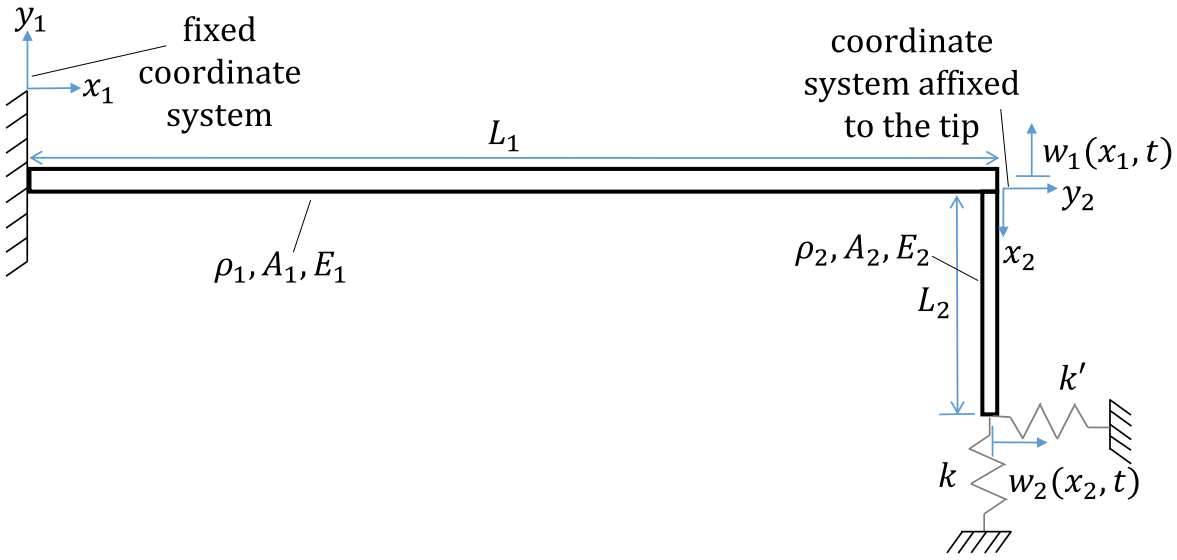

Figure 1. Cantilever sensor with an elastic tip in contact with an elastic substrate (modeled as linear springs). This system represents an L-shaped structure comprised of two E–B beams.

the advantages offered by imaging with qPlus sensors, researchers have achieved remarkable feats, including obtaining Angstrom-level spatial resolution by attaching a single molecule to the end of the sensing tip [18], and observing the signature of electron orbitals [19].

Jaquez-Moreno *et al* [20] introduced a new CR model for sensors with long, massive, rigid tips. The model was numerically verified in their work, and was later experimentally validated by Zimron-Politi and Tung [21]. The successful use of nano-needles and qPlus sensors in trolling mode, along with new theoretical CR models, paves the way for contact resonance trolling mode (CRTM). CRTM will allow advanced measurements of biological samples *in situ*, and will further improve AFM's current and successful use for health-care applications [22–24]. With the decreasing diameter of the tip, to allow for high spatial resolution imaging, and the extended length, to allow in-liquid measurements and perform invasive cell manipulation [25–27], the contribution of the flexibility of the tip becomes significant. In order to include the tip's flexibility, the system is modeled using a two beam layout, sometimes referred to as an L-shaped beam. The structural vibrations of frames and L-shaped beams has been the focus in a variety of fields and applications, such as microrobotics [28], micro electro mechanical systems (MEMS) [29, 30], and energy harvesting [31–33]. The frames have been studied in a general arbitrary configuration [34], and specifically in the L-shaped configuration analytically [35, 36] and numerically [37].

In this paper, a theoretical model for the flexural vibrations of an L-shaped beam fixed on one end and supported by two springs on the other end is developed. The procedure to generate the equation governing the natural frequencies of the coupled sensor-tip-sample system, known as the characteristic equation is outlined. Then, the orthogonality condition for the eigenmodes is derived, and a numerical experiment mimicking CR measurements is performed. The proposed model is used to predict sample stiffness with great success for two cases of long, elastic AFM tips. The orthogonality condition is also used to predict eigenmode veering and crossing, and is discussed in section 2.3.

2. Theory and model development

In this section, a theoretical model for a cantilever sensor equipped with a long, elastic tip is developed. The joint structure of the cantilever and tip results in an L-shaped beam sensor. The L-shaped beam sensor has one side securely fastened from displacements and rotations (fixed), and another side elastically supported by two linear springs (see figure 1). The L-shaped beam is modeled using two Euler–Bernoulli (E–B) beams connected by appropriate boundary conditions. Each of the E–B beams has one side fixed, relative to its own coordinate system. The beam with one side globally fixed represents the classic AFM cantilever beam, whereas the other beam, with one end elastically supported, represents the long elastic tip which can be used in trolling mode. In figure 1, the key parameters of the CR idealized model under investigation are illustrated. Small amplitude vibrations are assumed throughout this work. For clarity of nomenclature, the classic AFM cantilever beam is referred to as 'beam' and the elastic tip as 'tip'.

2.1. Flexural vibrations

With reference to figure 1, the flexural vibrations of the beam-tip-sample model are analyzed in the x_1-y_1 plane only. The beam is assumed to be of constant cross-sectional dimension with area A_1, length L_1, density ρ_1, and Young's modulus E_1. The tip is located at $x_1 = L_1$ and has a constant cross-section with area A_2, length L_2, density ρ_2, and Young's modulus E_2. The elastic substrate is modeled using two linear springs. The first is a vertical spring (normal) with stiffness k, and the second one is a lateral spring (tangential) with stiffness k'. The equation of motion for the transverse vibrations of the

beam is given by [38]:

$$\rho_1 A_1 \frac{\partial^2 w_1(x_1,\, t)}{\partial t^2} + E_1 I_1 \frac{\partial^4 w_1(x_1,\, t)}{\partial x_1^4} = 0, \tag{1}$$

where I_1 is the second area moment of inertia, and $w_1(x_1,\, t)$ represents the transverse displacement of the beam at a given location x_1 along the axis, and a specified time t. Similarly, the equation of motion for the transverse vibrations of the tip is defined in the tip coordinate frame. Due to the rotations of the tip coordinate system, the tip reference frame is non-inertial. An additional term is added to the right hand side of the equation due to the effects of the non-inertial reference frame. Translations of the tip coordinate system and axial effects are neglected. The equation of motion for the tip is given by:

$$\rho_2 A_2 \frac{\partial^2 w_2(x_2,\, t)}{\partial t^2} + E_2 I_2 \frac{\partial^4 w_2(x_2,\, t)}{\partial x_2^4} = -\rho_2 A_2 x_2 \ddot{\theta}, \tag{2}$$

where I_2 is the second area moment of inertia of the tip, and $w_2(x_2,\, t)$ represents the transverse displacement of the tip at a given location x_2 along the axis and a specified time t. $\theta(t) = \frac{\partial w_1(L_1,\, t)}{\partial x_1}$ is the slope at the end of the beam, $x_1 = L_1$, where the beam and tip are connected.

The coupling between the beam, tip, and the sample stiffness, are brought together into a single system model by manipulating equations (1) and (2), along with the following eight boundary conditions [38]:

$$w_1(0,\, t) = 0, \tag{3a}$$

$$\frac{\partial w_1}{\partial x_1}(0,\, t) = 0, \tag{3b}$$

$$E_1 I_1 \frac{\partial^2 w_1(L_1,\, t)}{\partial x_1^2} = -I_t \frac{\partial^3 w_1(L_1,\, t)}{\partial x_1 \partial t^2} - k' L_2^{\,2} \frac{\partial w_1(L_1,\, t)}{\partial x_1} - k' L_2 w_2(L_2,\, t) - \int_0^{L_2} \rho_2 A_2 x_2 \ddot{w}_2 dx_2, \tag{3c}$$

$$E_1 I_1 \frac{\partial^3 w_1(L_1,\, t)}{\partial x_1^3} = m_t \frac{\partial^2 w_1(L_1,\, t)}{\partial t^2} + k w_1(L_1,\, t), \tag{3d}$$

$$w_2(0,\, t) = 0, \tag{3e}$$

$$\frac{\partial w_2}{\partial x_2}(0,\, t) = 0, \tag{3f}$$

$$E_2 I_2 \frac{\partial^2 w_2(L_2,\, t)}{\partial x^2} = 0, \tag{3g}$$

$$E_2 I_2 \frac{\partial^3 w_2(L_2,\, t)}{\partial x_2^3} = k' w_2(L_2,\, t) + k' L_2 \frac{\partial w_1(L_1,\, t)}{\partial x_1}, \tag{3h}$$

where I_t is the rotational inertia of the sensing tip, and m_t is the total mass of the sensing tip. Equations (3*a*) and (3*b*), represent the fixed boundary condition on one side of the beam. Equations (3*c*) and (3*d*) represent the bending moment and shear forces at the beam end, respectively. Equations (3*e*) and (3*f*) represent the fixation of the tip to the beam in the tip coordinate frame. Equations (3*g*) and (3*h*) represent the bending moment and shear forces at the tip end, respectively. Due to the small displacement assumption, nonlinear terms which include multiplicative products of the beam deflection and tip deflection, such as the bending moment applied on the beam end, caused by the term $kw_1(L_1,\, t)w_2(L_2,\, t)$ are ignored. Furthermore, any effects due to axial deformation of the beam and tip are neglected.

Dimensional analysis of the two equations of motion and the boundary conditions allows identification of the non-dimensional parameters which will govern the problem:

$$\alpha = \frac{k}{k_c}, \quad \phi = \frac{k'}{k}, \quad \hat{I}_t = \frac{I_t}{\rho_1 A_1 L_1^{\,3}}, \quad \ell = \frac{L_2}{L_1},$$
$$\Delta = \frac{m_t}{\rho_1 A_1 L_1}, \quad R_d = \sqrt{\frac{E_1 I_1 \rho_2 A_2 L_2^{\,4}}{E_2 I_2 \rho_1 A_1 L_1^{\,4}}}, \tag{4}$$

where $k_c = \frac{3E_1 I_1}{L_1^3}$ is the static stiffness of the beam. R_d can also be written as: $R_d = \sqrt{\frac{k_c}{k_t} \cdot \Delta}$, where $k_t = \frac{3E_2 I_2}{L_2^3}$ is the static stiffness of the tip. R_d encapsulates the dynamic coupling effects between the beam and the tip by combining the beam and tip static stiffness ratio, multiplied by the mass ratio. For the limit of $E_2 \to \infty$ leading to $R_d \to 0$, the model reduces to the rigid tip model presented by Jaquez-Moreno *et al* [20]. The limit of the nondimensional sample stiffness $\alpha \to 0$ corresponds to the case of a freely vibrating L-shaped beam discussed by Oguamanam *et al* [34, 35]. This limiting case represents the situation where no contact between the sensor tip and the sample exists.

The solution for the equations of motion, presented in equations (1) and (2), is based on the assumption of a separable solution [38], such that $w_i(x_i,\, t) = L_i \cdot W_i(\zeta_i) \cdot e^{j\omega t}$ where $\zeta_i = \frac{x_i}{L_i}$ is the nondimensional length along the beam and the tip, and ω is the dimensional natural frequency. Substituting the ansatz of a separable solution into equations (1) and (2), and using the dimensional analysis, leads to two ordinary differential equations of fourth order, in the spatial dimensions ζ_1 and ζ_2, describing the eigenfunctions, or mode shapes, of the beam-tip-sample system:

$$W_1'''' - (\lambda_1 L_1)^4 \cdot W_1 = 0, \tag{5}$$

$$W_2'''' - (\lambda_2 L_2)^4 \cdot (W_2 + \zeta_2 \cdot W_1'(1)) = 0. \tag{6}$$

λ_i are the separation constants such that: $(\lambda_i L_i)^4 = \omega^2 (\rho_i A_i L_i^{\,4}) / (E_i I_i)$. Using the above relation also leads to the relation between the two separation constants: $\lambda_2 L_2 = \lambda_1 L_1 \sqrt{R_d}$. The general form of the spatial solution for the homogeneous equation (5) is:

$$W_1(\zeta_1) = C_1 \cos(\lambda_1 L_1 \cdot \zeta_1) + C_2 \sin(\lambda_1 L_1 \cdot \zeta_1) + C_3 \cosh(\lambda_1 L_1 \cdot \zeta_1) + C_4 \sinh(\lambda_1 L_1 \cdot \zeta_1), \tag{7}$$

and the general form of the spatial solution for the non-homogeneous equation (6) can be found using the method of undetermined coefficients [39]:

$$W_2(\zeta_2) = C_5 \cos(\lambda_2 L_2 \cdot \zeta_2) + C_6 \sin(\lambda_2 L_2 \cdot \zeta_2) + C_7 \cosh(\lambda_2 L_2 \cdot \zeta_2) + C_8 \sinh(\lambda_2 L_2 \cdot \zeta_2) - \zeta_2 \cdot W_1'(1). \tag{8}$$

Using the dimensional analysis and the separable solution, the nondimensional forms of the boundary conditions given in equation (3) are simplified to:

$$W_1(0) = 0, \tag{9a}$$

$$W_1'(0) = 0, \tag{9b}$$

$$W_1''(1) = (\lambda_1 L_1)^4 \hat{I}_t W_1'(1) - 3\alpha\phi\ell^2(W_2(1) + W_1'(1)) + (\lambda_1 L_1)^4 \Delta\ell^2 \int_0^1 \zeta_2 W_2 d\zeta_2, \quad (9c)$$

$$W_1'''(1) = (3\alpha - (\lambda_1 L_1)^4 \Delta) W_1(1), \quad (9d)$$

$$W_2(0) = 0, \quad (9e)$$

$$W_2'(0) = 0, \quad (9f)$$

$$W_2''(1) = 0, \quad (9g)$$

$$W_2'''(1) = 3\alpha\phi \frac{R_d^2}{\Delta}(W_2(1) + W_1'(1)). \quad (9h)$$

From the boundary condition equations (9*a*), (9*b*) and (9*e*) it can be shown that:

$$C_1 = -C_3, \; C_2 = -C_4, \text{ and } C_5 = -C_7. \quad (10)$$

Combining the general solutions given in equations (7) and (8), along with the boundary conditions given in equation (9), the eigenvalue problem (EVP), which governs the eigenmodes and eigenfrequencies of the system, can be formed. By performing algebraic manipulations, five linear homogeneous equations in C_m are obtained, i.e. the integration coefficients. These equations are expressed in matrix form as:

$$[M]_{5x5}\{q\}_{5x1} = \{0\}_{5x1}, \quad (11)$$

The elements of matrix M are given in appendix A, and $\{q\} = [C_3, C_4, C_6, C_7, C_8]^T$ is the vector of integration coefficients.

The solution to the EVP is obtained by setting the determinant of matrix M to zero, in order to find the non-trivial solution. This manipulation results in the characteristic equation of the system, which describes the relationship between the governing nondimensional parameters and the natural frequencies, functionally described by:

$$f(\lambda_1^n L_1, \alpha, \Delta, \hat{I}_t, \ell, \phi, R_d) = 0. \quad (12)$$

Here, λ_1^n is the wave number of the nth natural frequency and the remaining parameters are the non-dimensional quantities described previously. The characteristic equation can be solved for any of the countably infinite $\lambda_1^n L_1$ eigenvalues (EV) of the system.

2.2. Orthogonality condition

The orthogonality between any two eigenmodes is an important condition in the modal analysis of a system, and it can also be used to mass-normalize the eigenmodes [38]. A full derivation of the orthogonality condition is presented in appendix B, with the final condition given as:

$$\int_0^1 W_{1,r} \cdot W_{1,s} \cdot d\zeta_1 + W_{1,r}(1) \cdot \Delta \cdot W_{1,s}(1) + W_{1,r}'(1) \cdot \hat{I}_t \cdot W_{1,s}'(1) + \Delta\ell^2 \cdot \int_0^1 [W_{2,r} \cdot W_{2,s} + \zeta_2 \cdot (W_{2,r} \cdot W_{1,s}'(1) + W_{2,s} \cdot W_{1,r}'(1))] \cdot d\zeta_2 = \delta_{rs}. \quad (13)$$

δ_{rs} is the Kronecker delta, and r and s are subscripts describing any two eigenmodes. Equation (13) can be used to obtain the mass-normalized eigenmodes by solving the equation for the unknown integration coefficient in the case of r = s, as is standard practice in modal analysis [38].

2.3. Eigenmode veering and crossing and its effect on the CR measurements

Eigenmode veering or crossing is a phenomenon where a change in a single or multiple parameters of the system causes a change in the trajectory of the natural frequency loci [40]. For example, in CR measurements the in-contact resonance frequencies for a given set point force, which is related to the nondimensional sample stiffness α, are measured. The frequencies measured are related to specific modes, which for a simple cantilever probe can be related to the well-known bending modes of an Euler–Bernoulli beam. Using simple cantilever AFM probes, the transverse bending modes maintain their initial ordering with the change in α. Nonetheless, each mode shape evolves with the change in α while the eigenfrequency ordering remains in place.

For the cases discussed in this work, where a long elastic tip is used, other mode shapes are generated due to the tip's dynamics. Varying α can introduce eigenmode veering and crossing, which interferes with the tracking of a specific mode for contact resonance. The ability to track a specific mode with the change in the contact force is crucial for the accurate prediction of the sample's stiffness α. In the case of an eigenmode veering or crossing, if a CR frequency is associated with the wrong eigenmode the results may become erroneous.

The interaction between two or more frequency loci can take place in two forms In the first form, a crossing of the two frequency curves is witnessed, evidenced by a change in order between two eigenfrequencies. For example, assume that a certain eigenmode shape is associated with the lowest frequency for a specific value of the varying parameter. As the varying parameter is increased, the eigenmode shape now becomes associated with the 2nd lowest frequency. By plotting the eigenvalues or the eigenfrequencies as a function of the varying parameter, an abrupt crossing can be seen with the loci intersection. In the second form, the eigenmode veering, the two loci approach each other but diverge without intersecting. Nonetheless, the final result of the eigenmode veering interaction is the same as in the eigenmode crossing, a change in the eigenmode shape ordering. In the eigenmode veering case, the interaction between the two loci is continuous and without an actual intersection, and therefore more complicated to distinguish. Furthermore, the interaction in the eigenmode veering case occurs over a certain range of the varying parameter, and not at a specific value of the varying parameter, as in the eigenmode crossing case. Using traditional CR models and sensors, eigenmode veering and crossing is rarely, if ever, encountered.

Huang *et al* [40] developed a sensitivity function which allows one to accurately distinguish between eigenmode veering and crossing. Furthermore, the sensitivity function is used in this work to track the mode shape evolution as it changes with the increase in α. The sensitivity function uses

the inner product between two eigenvectors, $\mathbf{\Phi}_r$ and $\mathbf{\Phi}_s^0$:

$$S_{r,s} = \langle \mathbf{\Phi}_r, \mathbf{\Phi}_s^0 \rangle, \tag{14}$$

where $\mathbf{\Phi}_s^0$ is the s^{th} normalized eigenvector for the case of the minimum value of the varying parameter, and $\mathbf{\Phi}_r$ is the rth normalized eigenvector which varies for different values of the varying parameter. By plotting $S_{r,s}$ as a function of the parameter causing the interaction, the two different types of interactions: the eigenmode veering or crossing, can be distinguished. In the case of an eigenmode crossing between modes r and s, the value of $S_{r,s}$ will change from zero right before the crossing (recall that any two modes are orthogonal), to a value of one immediately after the crossing. This indicates that mode shape $\mathbf{\Phi}_r$, which was orthogonal to $\mathbf{\Phi}_s^0$ before the crossing, has becoming similar to $\mathbf{\Phi}_s^0$ after the crossing. In the case of an eigenmode veering, the two modes interact over a certain range in a continuous fashion. In this veering range, the mode shapes of the two veering modes become a combination of the two interacting modes, leading to a continuous change in the value of $0 < S_{r,s} < 1$. As the veering takes place, both eigenmodes are distinctly altered, as compared to their shapes prior to the veering.

In this work, eigenmode veering and crossing is examined while varying the nondimensional sample stiffness α. The orthogonality condition given in equation (13) is implemented as a sensitivity function to investigate possible changes between eigenmodes used in the aforementioned CR procedure. Here, the mode shape $\mathbf{\Phi}_s^0$ corresponds to the out-of-contact mode shape, or the $\alpha = 0$ mode shape. Implementing the orthogonality condition between $W_{1,r}$, $W_{2,r}$ and $W_{1,s}^0$, $W_{2,s}^0$ leads to:

$$\begin{aligned}\tilde{S}_{r,s} = &\int_0^1 W_{1,r} \cdot W_{1,s}^0 \cdot d\zeta_1 + W_{1,r}(1) \cdot \Delta \cdot W_{1,s}^0(1) \\ &+ W_{1,r}'(1) \cdot \hat{I}_t \cdot W_{1,s}{}'^0(1) \\ &+ \Delta \ell^2 \cdot \int_0^1 [W_{2,r} \cdot W_{2,s}^0 + \zeta_2 \cdot (W_{2,r} \cdot W_{1,s}{}'^0(1) \\ &+ W_{2,s}^0 \cdot W_{1,r}'(1))] \cdot d\zeta_2,\end{aligned} \tag{15}$$

where $\tilde{S}_{r,s}$ is the sensitivity function in integral form.

The use of the inner product sensitivity function, given in equation (14), can be implemented only when the eigenvectors are produced by numerical tools, such as a Finite Element Analysis, and are then normalized by the norm of the vector. In the case of a real world contact resonance experiment, the integral form of the sensitivity function, given in equation (15), can be used. This form is based on the presented theoretical model. This will allow researchers to predict possible eigenmode veering and crossing in any α domain, without the need to use finite element analysis for a wide range of α. Unlike simple cantilever beams, the orthogonality conditions in the case of an L-shaped beam must include the effects from the beam and elastic tip, along with the natural boundary conditions of the problem. Discretizing the continuous solutions given in equations (7) and (8) into a column vector format, and performing the dot product between two different modes ($r \neq s$), it is found that the solution is not orthogonal, unless all the effects considered in the derived orthogonality condition (given in equation (15)) are implemented. Thus, utilizing the orthogonality condition as a sensitivity function for determining eigenmode veering and crossing offers a strong advantage in terms of computational efficiency. In the case of a long massive rigid tip, as discussed in [20], the orthogonality condition will include the effects from the natural boundary conditions of tip mass and rotational inertia, and is also different than the simple case of a cantilever beam without any natural boundary conditions.

2.4. Sample stiffness identification procedure

In CR, the experimental natural frequencies are converted to the eigenvalues of the system using the dispersion relation:

$$f_n = \frac{(\lambda_1^n L_1)^2}{2\pi} \sqrt{\frac{E_1 I_1}{\rho_1 A_1 L_1^4}}. \tag{16}$$

Zimron-Politi and Tung [21] proposed to rewrite the dispersion relation in the form:

$$\lambda_1^n L_1 = \sqrt{f_n \cdot \tilde{C}}, \tag{17}$$

thus, defining a new system parameter $\tilde{C}$. $\tilde{C}$ cannot be determined by using the fixed-free eigenvalues, as in common CR practice, where the tip mass and rotational inertia are ignored. The out-of-contact, or the 'free' frequencies, provide information about the sensor related parameters of the system. The out-of-contact characteristic equation is obtained by considering the case of $\alpha = 0$, and is reduced to a function of 5 system parameters, functionally described as follows:

$$f(\lambda_1^n L_1, \Delta, \hat{I}_t, \ell, R_d) = 0. \tag{18}$$

Plugging equations (17) into (18) will lead to an equation with 5 unknown system parameters, along with an experimental frequency. A similar scheme was introduced in [21] considering the long, massive, rigid, tip model out of contact. In order to estimate the system parameters, they used information from 3 freely vibrating transverse eigenfrequencies of the sensor in order to determine the 3 unknown system parameters of their system: Δ, $\hat{I}_t$, and $\tilde{C}$, which was denoted as the 3-Mode approach. In the case presented here, due to the elasticity of the tip, the freely vibrating sensor problem results in the following 5 unknown system parameters: Δ, $\hat{I}_t$, $\tilde{C}$, R_d, and ℓ. In order to estimate the 5 unknown system parameters 5 freely vibrating eigenfrequencies are used. This complex, highly nonlinear set of 5 equations is challenging for numerical solution of similar form, i.e. a 5-Mode approach. Furthermore, one may also use other measurements to estimate some of the system parameters. For example, an estimation for $\ell = \frac{L_2}{L_1}$ by a scanning electron microscope (SEM) is relatively simple, and will reduce the problem to 4 unknowns. For some tip geometries, a relation between Δ, $\hat{I}_t$, and ℓ can be analytically derived, which will further reduce the dimensionality of the problem. For example, considering a cylindrical tip, the rotational inertia of the sensing tip is given by $I_t = \frac{1}{3} m_t L_2^2$ at the beam and tip interface. Therefore, $\hat{I}_t$ can be expressed as a function of Δ and ℓ: $\hat{I}_t = \ell^2 \frac{\Delta}{3}$.

For typical optical lever based AFM systems, the detection of eigenmodes consisting primarily of tip motion is unlikely,

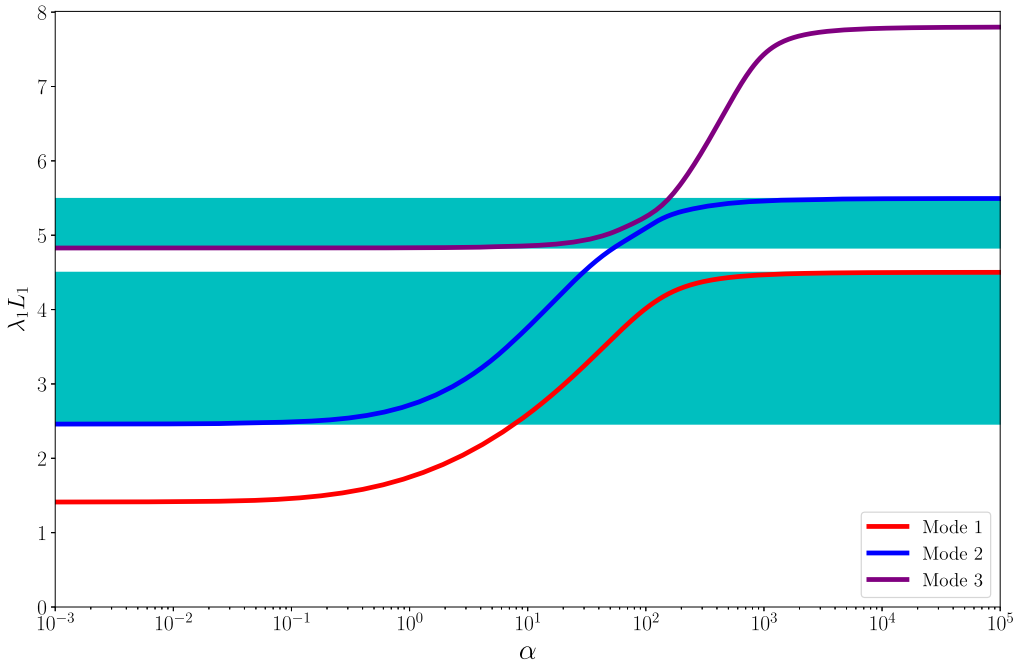

Figure 2. Eigenvalue loci showing multiple α solutions in blue background regions, with $\Delta = 0.5$, $\hat{I}_t = 0.005$, $R_d = 0.5$, $\ell = 0.5$, and $\phi = 0.8$.

especially if the tip mass is negligible relative to the mass of the cantilever beam. In such a case, a higher frequency bandwidth must be used to measure all the required freely vibrating eigenfrequencies, resulting in a more elaborate experimental setup. Furthermore, the model derived in this work is based on the Euler–Bernoulli beam equation, which ignores the rotational inertia of the cross-section and shear effects, thereby performing better for lower modes where these effects are negligible. With the two considerations described above, along with the complexity of solving a system of 5 highly nonlinear equations, reducing the dimensionality of the free system to 3 free measurements and 3 unknown system parameters is proposed. In [21], a graphical approach was also used to find the system parameters and to ensure a single solution is found, thus illustrating another advantage of using a 3-Mode approach. In order to reduce the dimensionality of the free system discussed here, throughout this work it is assumed that $\ell = \frac{L_2}{L_1}$ is known (as if it was measured by an SEM), and the analytical relation for a cylindrical tip: $\hat{I}_t = \ell^2 \frac{\Delta}{3}$ is used. Following the above 2 procedures, a measurement of 3 free eigenfrequencies will determine the remaining 3 unknown system parameters: Δ, $\tilde{C}$, and R_d. Note that the use of any number of free eigenfrequencies for the determination of the system parameters is not limited to the lowest free eigenfrequencies. That is, any free eigenfrequency can be used, regardless of the mode shape (beam dominant or tip dominant) and the ordering.

Once all system parameters that can be identified using free frequencies are estimated, one can proceed to the in-contact measurements and estimation of the remaining parameters. For the in-contact cases, the remaining two unknown parameters in the characteristic equation are α and ϕ which can be determined either by a single mode prediction, or by a multi-modal prediction. In a single mode prediction, ϕ is assumed to be known and may use any mode to calculate α. In a multi-modal prediction, both α and ϕ are solved for simultaneously [41], by using two different eigenfrequencies. Throughout this work, both the single and multi-modal predictions are demonstrated for the different examples.

The characteristic equation functionally given in (12) is a quadratic equation in α, therefore resulting in two solutions. The phenomenon of having multiple α solutions was discussed theoretically in [20], and proven experimentally in [21]. The solution to the quadratic equation: $c_2\alpha^2 + c_1\alpha + c_0 = 0$ is the well-known quadratic formula: $\alpha_{1,2} = \frac{-c_1 \pm \sqrt{c_1^2 - 4c_2c_0}}{2c_2}$. Investigating the possible α solutions using physically realistic system parameters shows that two real solutions are always found.

Consider the case presented in figure 2 for an eigenvalue greater than the value of the minimum found for mode 2 (the freely vibrating 2nd mode), and less than the maximum value found for mode 1 (the high sample stiffness value). In the described region, i.e. in the lower blue background range, two eigenmodes exist, one with a low α value corresponding to mode 2, and one with a higher α value corresponding to mode 1. That is, in the blue background range, two positive α solutions exist corresponding to the $\pm$ solutions of the quadratic equation. Similarly, in the upper blue background range, two positive α solutions exist, one for mode 3 (lower α value), and the second for mode 2 (higher α value). Outside of the blue regions, one negative α solution and one positive α solution are obtained. The negative α solution is disregarded as it is not physically meaningful.

3. Numerical experiments

In CR experiments, the measured freely vibrating and in-contact natural frequencies are used, along with a theoretical model, to estimate the sample stiffness. Then, a contact

Table 1. qPlus sensor dimensions and mechanical properties used in the FE model.

Quartz prong		Tungsten tip	
E_1	80 GPa	E_2	345 GPa
ν_1	0.17	ν_2	0.28
ρ_1	2650kgm^{-3}	ρ_2	19300 kgm^{-3}
L_1	2.357 mm	L_2	1.186 mm
h	0.2134 mm	d	0.1 mm
b	0.127 mm	L_e	0.15 mm

ν_i are the Poisson ratios, h and b are the thickness and width of the quartz beam respectively, d is the diameter of the tungsten tip, and L_e is the length of the etched section of the tip. In the FE model, for the etched section, the tip diameter reduces from the nominal diameter d to a diameter of 0.01 mm due to the size of the other components in the model and mesh considerations.

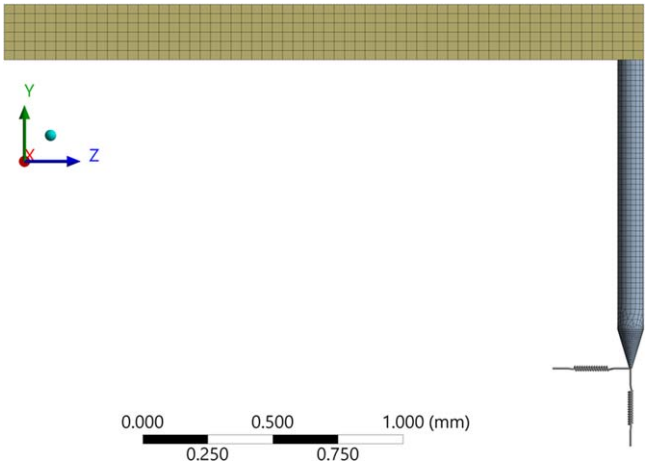

Figure 3. FE model of the qPlus sensor with a tungsten tip.

mechanics model is used to calculate the reduced modulus, which is a series combination of the indentation modulus of the sample and tip. In order to verify the new proposed model, a numerical experiment in which data from a finite element (FE) modal analysis is used in lieu of a real AFM experiment. This allows one to perform an estimation of the FE assigned sample stiffness, using the modal frequencies and the proposed model. Then, the relative error between the estimated stiffness and the assigned stiffness is calculated, based on the proposed CR model and system parameter identification scheme. Thus, the numerical experiment allows one to isolate the proposed CR model accuracy from the additional contact mechanics and experimental setup errors. The percent of relative error is calculated as follows:

$$\mathrm{P.E} = \frac{\alpha_{\mathrm{ETM}} - \alpha_{\mathrm{FE}}}{\alpha_{\mathrm{FE}}} \times 100, \tag{19}$$

where α_{ETM} is the nondimensional sample stiffness estimated by the elastic tip model (ETM), and α_{FE} is the sample stiffness assigned in the FE model normalized by the calculated static stiffness of the sensor.

In the following numerical experiments, previously published sensors that contain significant tip modifications are modeled. The FE model includes an L-shaped elastic beam fixed at one end and elastically supported by two springs on the other end, representing the sample stiffness. The FE simulations were performed using ANSYS commercial software with a parametric study varying the elastic support of the tip.

In a homogeneous material, the normal sample stiffness k and the lateral sample stiffness k' are related via the Poisson ratio ν, such that [42, 43] $\frac{k'}{k} = \phi = 2\frac{1-\nu^2}{(1+\nu)(2-\nu)} = 2\frac{1-\nu}{2-\nu}$. For realistic values of the Poisson ratio given by $0 < \nu < 0.5$, ϕ is limited to $2/3 < \phi < 1$. Throughout this work, $\phi = \frac{k'}{k} = 0.8$ is assigned in the numerical experiments, which represents a Poisson's ratio of $\nu = 1/3$.

The nondimensional sample stiffness α is the varying parameter in the parametric study and is controlled by adjustment of the normal spring stiffness supporting the L-shaped beam. For all cases discussed in this work, the static stiffness of the cantilever beam is used to normalize the value of the normal spring in the FE model. A preliminary static analysis is performed to find the static stiffness k_c of the beam. A unit load F_{app} is applied at the tip end, in the direction along the tip, for the free case (no springs attached to the tip), and the directional deflection δ at the tip end is measured. The static stiffness is then calculated such that: $k_c = \frac{F_{\mathrm{app}}}{\delta}$. The sample stiffness is varied in an actual experimental setup by changing the amount of force pressing the sensor tip against the sample, increasing the contact area and the corresponding sample stiffness. Each of the numerical experiments is described in more detail in the next sub-sections.

3.1. qPlus sensor

In this section, the numerical experiment performed using an AFM qPlus sensor is described. The qPlus sensor is built from a quartz tuning fork (QTF) and may be modified with a variety of tips. In the numerical experiment discussed here, a tungsten needle is assumed as a probing tip. The setup describe by Yamada *et al* [44] to perform nano-lubrication measurements is used in order to simulate the contact resonance setup. The dimensions and mechanical properties used in the simulation are presented in table 1, and the nondimensional sample stiffness is varied between $10^{-3} < \alpha < 10^5$, covering a wide range of possible sample stiffnesses.

A solid hex dominant mesh is used in the FE model (see figure 3), and the resulting modal frequencies are sorted for the in-plane vibration modes. In an AFM experiment, one must use both transverse and lateral channels to properly identify the transverse modes. The processing of out-of-plane eigenfrequencies using the ETM model can result in significant inaccuracies. An additional analysis is performed with the springs set to zero stiffness, corresponding to the out-of-contact freely vibrating case. The lowest 3 free eigenfrequencies are used to determine the system parameters as described in section 2.4. The resulting system parameters used in this work are presented in table 2, along with the nominal values. Finally, each case's frequencies are used as input for the theoretical model to predict the nondimensional sample stiffness α using equation (12). Results are presented in section 4.

Table 2. qPlus sensor system parameters as calculated using the nominal values and the 3-Mode approach with 2 additional assumptions.

Source of data	Δ	$\hat{I}_t$	R_d	ℓ	$\tilde{C}$ (sec)
Nominal values	1.0193	0.0792	0.7469	0.4829	1.1206×10^{-4}
Three transverse modes (3-Mode approach)	0.8931	0.0825	0.7798	0.5264	1.1165×10^{-4}

For the nominal value of the tip length to cantilever length ratio, $\ell = \frac{L_2}{L_1}$ is used, whereas in the 3-Mode approach $\ell = \frac{L_2 + h/2}{L_1}$ is used to simulate an SEM measurement.

Table 3. Nano-needle sensor dimensions and mechanical properties used in the FE model.

Silicon sensor		Platinum tip	
Orthotropic material properties. See notes for details		E_2	168 GPa
		ν_2	0.284
ρ_1	2330 $\frac{\text{kg}}{\text{m}^3}$	ρ_2	21450 $\frac{\text{kg}}{\text{m}^3}$
L_1	125 μm	L_2	60 μm
h	2.1 μm	d	0.6 μm
b	25 μm		

Material properties used to describe the single crystal silicon sensor [45]. Material axes are given in figure 4. $E_x = E_z = 169.7$ GPa, $E_y = 130.4$ GPa, $\nu_{xy} = \nu_{zy} = 0.362$, $\nu_{yz} = \nu_{yx} = 0.278$, $\nu_{xz} = \nu_{zx} = 0.061$, $G_{xy} = G_{yz} = 80.0$ GPa, $G_{zx} = 51.0$ GPa.

3.2. Nano-needle sensor

Nano-needles are very thin and long extensions fabricated onto traditional AFM cantilever sensors. In this numerical setup, the experimental setup used in [8], using a silicon sensor and a platinum needle tip, is mimicked. The dimensions and mechanical properties used are presented in table 3, and the nondimensional sample stiffness is varied between $10^{-4} < \alpha < 10^3$.

In this case, due to the large dimensional differences between the cantilever and the needle tip, a solid hex dominant mesh is used for the silicon cantilever and Timoshenko beam elements are used to model the platinum needle tip (see figure 4). The needle tip has a constant cross-section and length to thickness ratio of 100 and is ideal for beam-type elements. Once again, the resulting modal frequencies are sorted for the in-plane vibration modes, and the 3-Mode approach is used to identify the system parameters. The resulting system parameters for the nano-needle are presented in table 4, along with the nominal values.

The use of nano-needles for sample property estimation may be limited by additional factors, including the axial stiffness of the needle tip and buckling of the tip. In this numerical setup, the axial stiffness of the tip is more than two orders of magnitude larger than the bending stiffness of the cantilever, so it is concluded it is well-suited for property estimation. Buckling of the needle tip can limit the applied load on the sample, but is also a function of the varying sample stiffness, as it alters the boundary conditions of the tip. In this work, it is assumed that no buckling is present, and the focus is placed on the vibration analysis of the system. Buckling of needle tips has been studied in [46].

The discrepancies reported in tables 2 and 4 between the nominal and the calculated values can be explained due to the deviation between the theoretical model and the numerical experiment setups. Such deviations may include: geometric simplifications, material model (for the nano-needle case), and neglecting nonlinear and axial effects. Furthermore, the use of the 3-Mode approach allows one to find an equivalent system using the presented theoretical model, that describes the experimental system in use, and results in equivalent free frequencies.

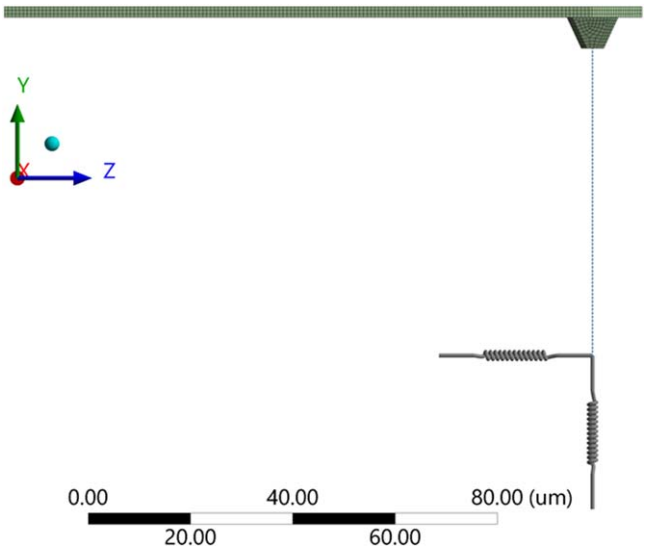

Figure 4. FE model of the silicon sensor with platinum needle tip. The Orthotropic material properties of the silicon sensor are given in the coordinate system shown at the bottom right corner.

4. Results and discussion

Using the presented ETM and the scheme for identifying the system parameters, both described in this work, the nondimensional sample stiffness α will now be predicted based on the numerical experiment eigenfrequencies, as is common in contact resonance practice. The eigenfrequencies are converted to eigenvalues using equation (17) and the calculated system parameter $\tilde{C}$. Then, the ETM characteristic equation in-contact, functionally presented in equation (12), is used with the remaining system parameters: Δ, $\hat{I}_t$, R_d, and ℓ, along with the eigenvalues obtained from equation (17). The prediction of α is demonstrated using a single mode prediction, to simplify the estimation procedure, for the qPlus sensor case in the next section by assuming $\phi = 0.8$. In the nano-needle case, the estimation is compared using a single and multimodal prediction scheme. Once α is estimated, the percent of relative error compared to the assigned stiffnesses from the finite element model is calculated using equation (19).

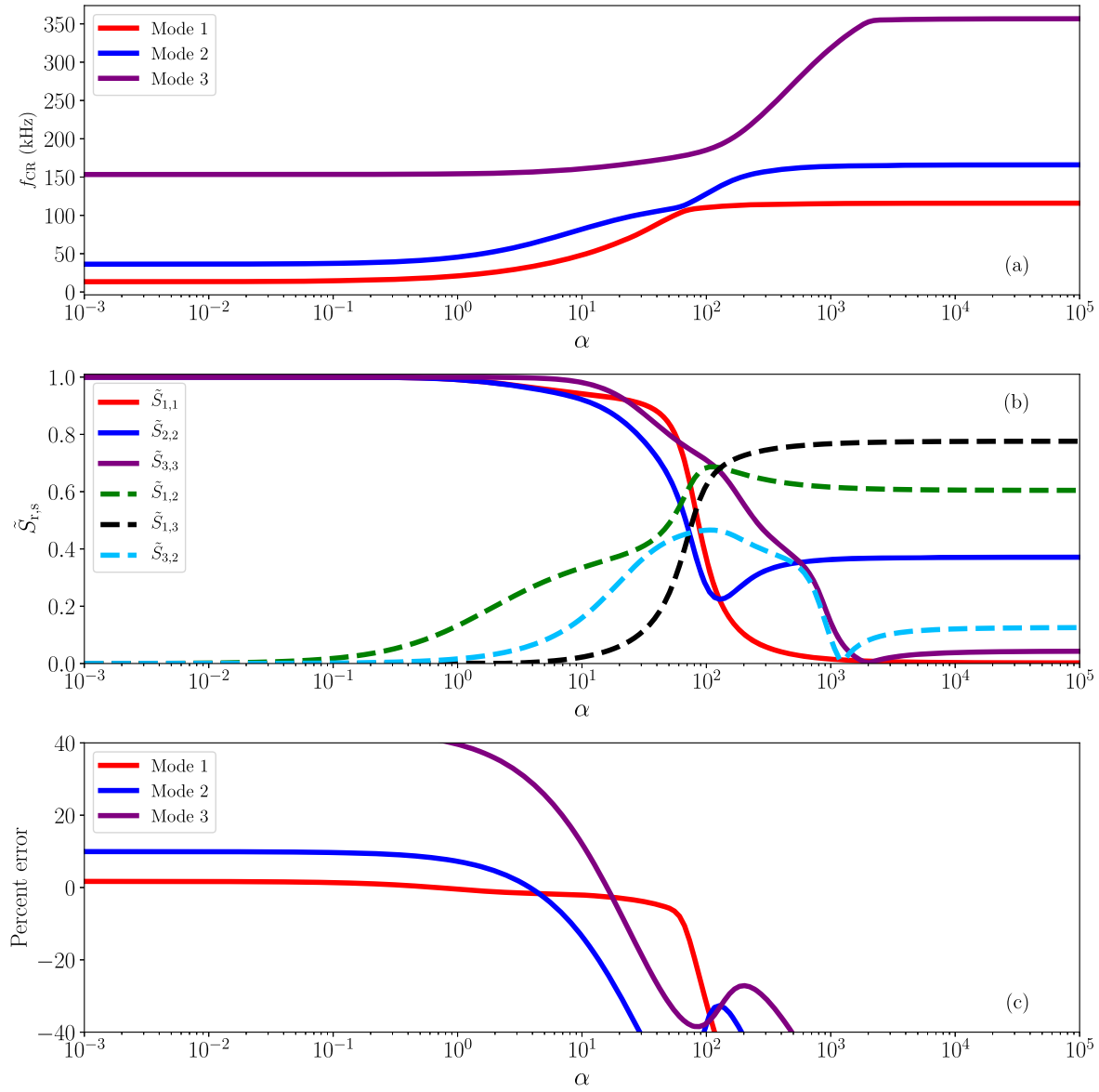

Figure 5. (a) FE numerical experiment results for the qPlus sensor. (b) Eigenfunction sensitivity showing complex interactions between the three lowest modes. (c) The percent of relative error of the single mode α predictions.

Table 4. Nano-needle system parameters as calculated using the nominal values and the 3-Mode approach with 2 additional assumptions.

Source of data	Δ	$\hat{I}_t$	R_d	ℓ	$\tilde{C}$ (sec)
Nominal values	0.0238	0.0018	2.7999	0.4800	1.9245×10^{-5}
Three transverse modes (3-Mode approach)	0.0185	0.0015	2.8433	0.4884	1.8976×10^{-5}

For the nominal value of the tip length to cantilever length ratio, $\ell = \frac{L_2}{L_1}$ is used, whereas in the 3-Mode approach $\ell = \frac{L_2 + h/2}{L_1}$ is assumed to simulate an SEM measurement.

4.1. qPlus sensor numerical experiment results

In figure 5(a), the lowest three transverse eigenfrequencies from the FE modal analysis, denoted by f_{CR}, are presented as a function of the nondimensional sample stiffness α. The 3 different modes are denoted 'Mode 1', 'Mode 2', and 'Mode 3' for simplicity. Recall that the mode shape associated with 'Mode 1', for example, with a low α value can become the second lowest eigenfrequency, as opposed to the lowest frequency, due to eigenmode veering or crossing. Using traditional CR with conventional cantilever geometries, eigenmodes transform due to sample stiffness changes, but never lose their initial ordering. A certain interaction between the two lowest eigenfrequencies can be observed around $\alpha = 50$ and is further examined by using the eigenfunction

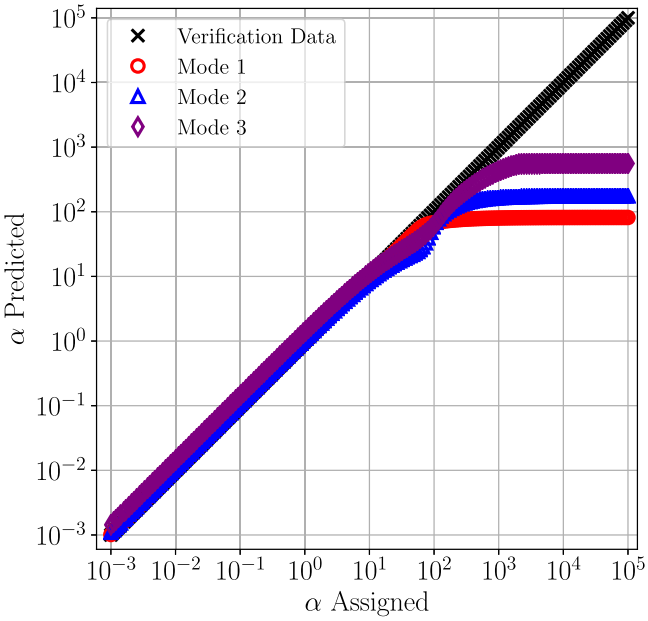

Figure 6. Elastic Tip Model predictions for the three lowest modes. Results are presented for the qPlus sensor case using single mode predictions (assuming $\phi = 0.8$).

sensitivity results presented in 5b. The sensitivity function results present a complex interaction, possibly between all 3 modes considered in the region $10^0 < \alpha < 10^3$. A clear determination of the veering or veerings is not achieved in this example. Nonetheless, by considering the changes in the relative error of the *r*th mode, and comparing it to the changes in the eigenfunction sensitivity of the $\tilde{S}_{r,r}$, a positive correlation is found. Thus, the prediction quality decreases for the *r*th mode when the eigenfunction sensitivity $\tilde{S}_{r,r}$ starts decreasing from a value of one. It is proposed that this phenomenon occurs when the mode shape starts deviating from the out-of-contact mode shape, indicative of an eigenmode veering, rather than a shift resulting from a change in sample stiffness. Given that eigenmode veering is a gradual, continuous transition spanning a specific region, the mode shapes progressively diverge. Since the system parameters were derived from the out-of-contact modes, any dissimilarity between the in-contact modes and their out-of-contact counterparts could potentially lead to inaccurate prediction of the sample stiffness. The foundation of contact resonance originally rested on the examination of the shift in eigenfrequencies between out-of-contact and in-contact states for a particular eigenmode. In this study, it is imperative to consider eigenmode veering and crossing to maintain the correlation between out-of-contact and in-contact eigenfrequencies of the same eigenmode.

For the third lowest eigenfrequency, a sharp change in slope is seen in the eigenfrequency versus α curve around $\alpha = 2000$ and may also be associated with eigenmode veering or crossing with higher modes. Higher eigenmode interactions can occur indefinitely, therefore the three lowest eigenfrequencies are focused on. These three frequencies are also the most widely used eigenfrequencies in CR and are practically observable using current AFM or qPlus sensor setups.

Due to the very high static stiffness of the Quartz prong, only very low α values are practical for nano level experiments. For example, if a tungsten tip radius of $R = 100$ nm [47] is considered, a reduced modulus of $E^* = 100$ GPa, and the Hertz contact mechanics model [48], it will require 0.1 N of force to reach an α of approximately 50, which is not suitable for nano-mechanical measurements. Nonetheless, the estimation will be continued for the sake of the analysis, and to gain a better understanding of the effects of eigenmode veering and crossing on the estimation, which occur at a high α value in this example.

Next, the single mode prediction of the nondimensional sample stiffness α is presented in figure 6, and the corresponding relative error in figure 5(c). The results show that the prediction using mode 1 is excellent for $\alpha < 10^2$, with the error limited to about $\pm 10\%$. The prediction using mode 2 shows excellent results for $\alpha < 10$. Using mode 3, the prediction does not produce adequate results in this case. A possible reason for the under performance of mode 3 prediction is the use of an Euler–Bernoulli (E–B) model for the description of a thick beam. As discussed in section 2.4, the E–B model neglects the rotational inertia of the cross-section and shear effects. The QTF's cross-section is relatively thick compared to its width, and will therefore be more affected by the neglected rotational inertia and shear effects, especially in higher modes.

In this section, a single-mode prediction of α is performed by assuming a known ϕ value. As ϕ is only a function of the Poisson ratio, as discussed at the beginning of section 3, it is bounded in the range of: $2/3 < \phi < 1$. It is found that a $\pm 10\%$ error in the estimation of ϕ will cause a change in the reported relative error of about $\pm 4\%$ using mode 1, and about $\pm 6\%$ using mode 2 at most. If no information is available on the value of ϕ (or the Poisson ratio) of the sample, it is recommended to use a multi-modal approach, as demonstrated next in the Nano-needle numerical experiment.

4.2. Nano-needle numerical experimental results

The numerical experiment results for the nano-needle sensor are presented in figure 7(a) for the lowest three transverse eigenfrequencies, denoted 'Mode 1', 'Mode 2', and 'Mode 3'. In this case, it is observed that the two lowest eigenfrequencies interact twice with each other around $\alpha = 6 \times 10^{-4}$, and then again around $\alpha = 0.4$, while the third lowest eigenfrequency does not undergo an interaction with other eigenmodes. Both interactions of mode 1 and mode 2 are eigenmode veerings, as a continuous change in the eigenfunction sensitivity is presented in figure 7(b). In figures 7(c)–(q), equations (7) and (8) are employed to plot the mode shapes for the three lowest eigenfrequencies, for different α values. To visualize the two veerings, multiple α values are considered: before the first veering, during the first veering, after the first and before the second veering, during the second veering, and after the second veering. The first and second eigenvectors associated with the lowest α value are represented by solid red and blue lines, respectively. The first eigenvector, presented in figure 7(c), is driven mainly by the tip motion, whereas the second eigenvector, presented in

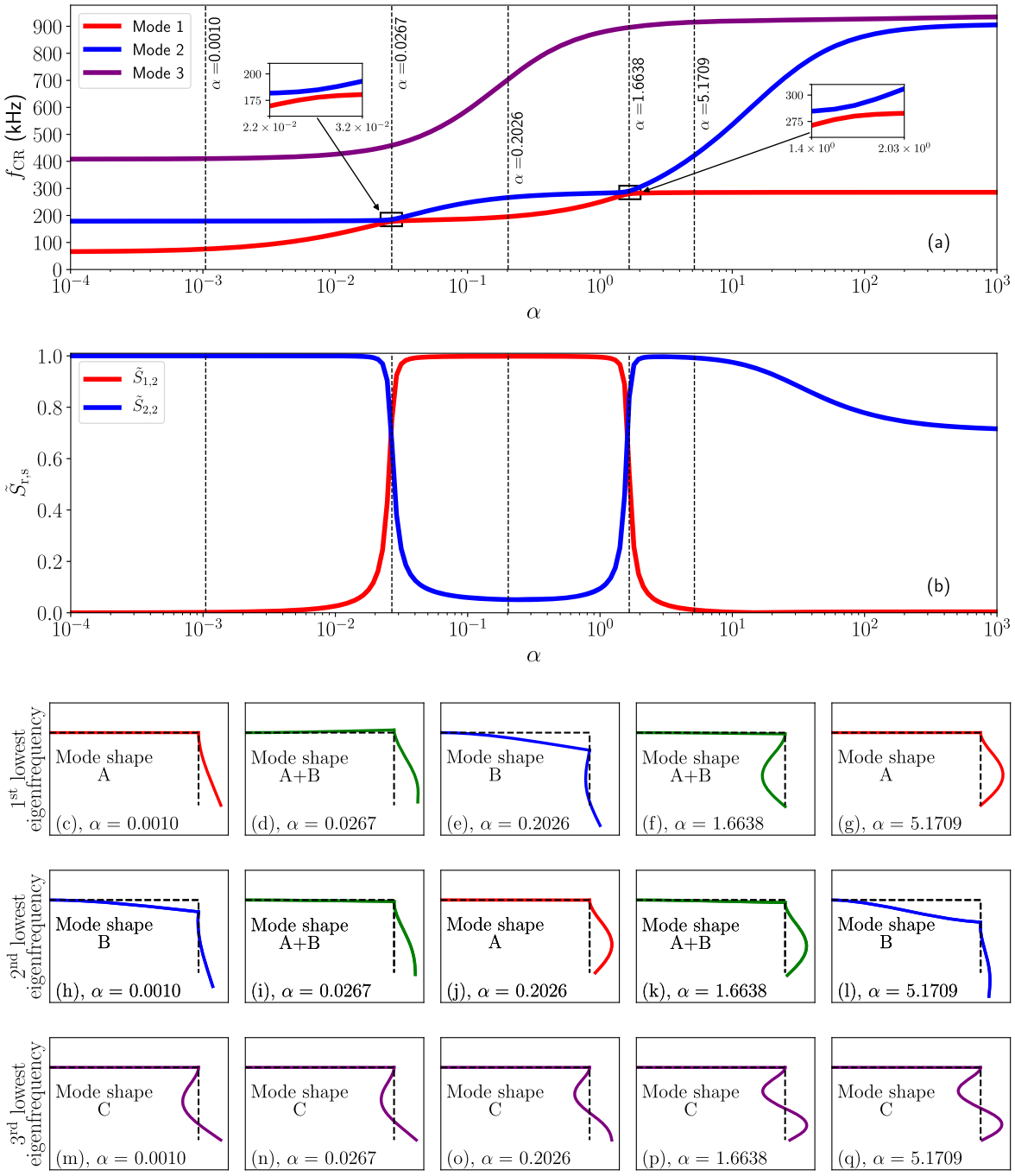

Figure 7. (a) FE numerical experiment results for the nano-needle sensor. Zoomed-in images show veerings of the two curves. (b) Eigenfunction sensitivity showing the two eigenmode veerings between mode 1 and mode 2. (c)–(g) The mode shape corresponding to the lowest eigenfrequency at different α values. (h)–(l) The mode shape corresponding to the second lowest eigenfrequency at different α values. (m)–(q) The mode shape corresponding to the third lowest eigenfrequency at different α values.

figure 7(h), is a combination of both the beam and tip. The eigenvectors interact during the veerings and create unique shapes which are a combination of both eigenvectors in the veering range (for each of the veering cases). After the first veering and before the second one, it is observed that the eigenvectors have switched order (see figure 7(e) and (j)). The mode shape associated with the 1st lowest eigenfrequency at $\alpha = 0.0010$ is denoted as mode shape A, and the 2nd lowest eigenfrequency at $\alpha = 0.0010$ is denoted as mode shape B. For the mode shapes presented in figure 7(c)–(l), the above definition is used to track a specific mode shape during the modes interaction.

Next, the single and multi-modal predictions of the non-dimensional sample stiffness α is presented in figure 8(a) and the corresponding relative error in figure 8(b). The single mode prediction results using mode 1 and mode 3 show excellent performance in the range of $\alpha < 30$, with mode 2 performing very good for a similar range. The effect from eigenmode veering

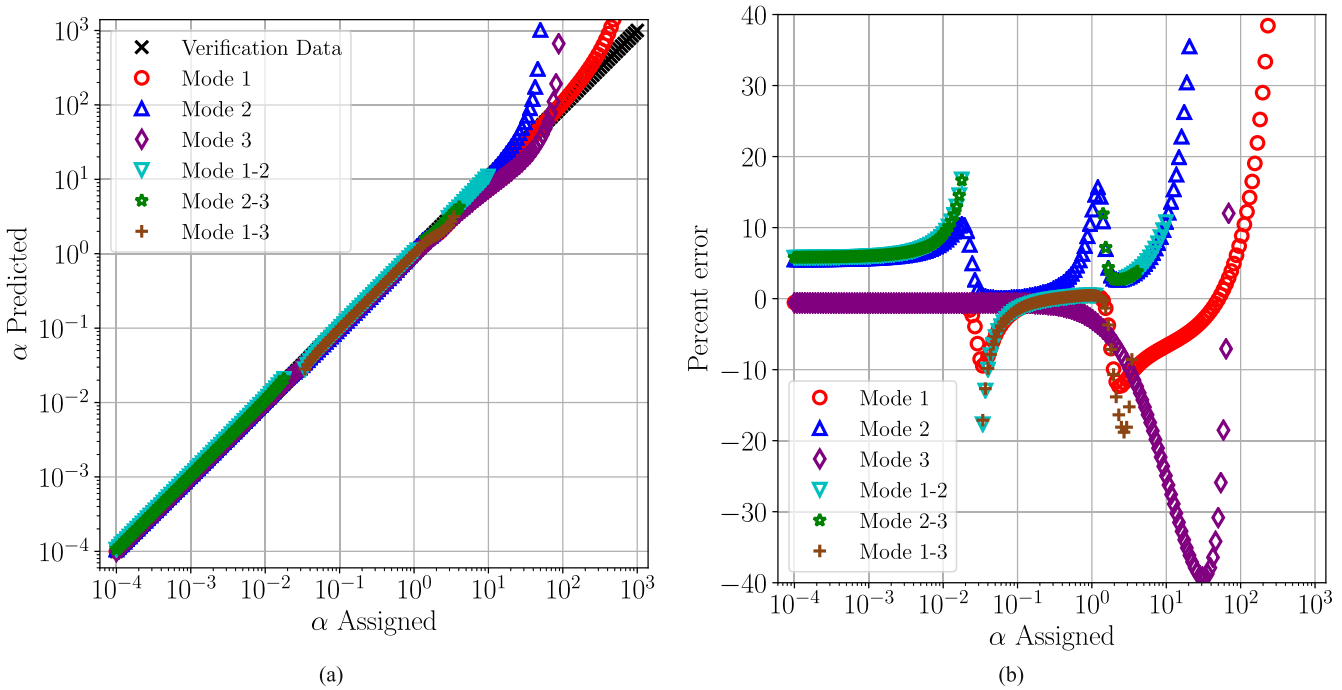

Figure 8. Elastic Tip Model predictions for the three lowest modes, compared to the assigned alpha values in the FE model. Result (a) and percent of relative error (b) presented for the nano-needle case. Mode $1/2/3$ are the results for the single mode prediction. Mode r–s is the result for a multi-modal prediction using data from mode r and mode s.

causes a change in the prediction, observable mainly in the veering range. In the multi-modal prediction analysis, the solutions are limited to physically meaningful solutions, i.e. $\alpha > 0$ and $2/3 < \phi < 1$. The multi-modal prediction using modes r and s is denoted as: mode r–s. The prediction error of mode 1–2 follows the error of the single mode 2 prediction, thus the multi-modal approach is affected more by the mode with the larger error. As mode 1 and mode 2 undergo eigenmode veering with each other, the multi-modal prediction using mode 1–2 does not fail as the information is maintained within the couple. Nonetheless, within the eigenmode veering ranges, the multi-modal prediction does fail, similarly to the single mode prediction. The mode 2–3 prediction performs similarly to the mode 1–2 prediction before the first veering, and after the second veering. The similarity can be explained due to the fact that both mode 1 and mode 3 perform better than mode 2 in the single prediction. Therefore, the multi-modal prediction error is dominated by the mode with the larger error, i.e. mode 2. Between the first veering and the second veering of modes 1 and 2, the mode 2–3 prediction fails while the mode 1–3 prediction performs excellent. Outside of the discussed range, the mode 1–3 prediction fails. After the second veering, mode 3 lacks sufficient measurement sensitivity [49] (different than the eigenfunction sensitivity), as the single mode prediction underperforms as well.

Before the first veering both mode 1 and mode 3 show excellent single mode prediction performance, and therefore it was expected that the mode 1–3 multi-modal prediction also perform well. This discrepancy can be explained by further investigation of the specific mode shapes. The mode combination that does not yield a solution is more suitably named mode A–C, rather than mode 1–3. After the first veering the mode B–C does yield good results. By considering the mode shapes A and C, it is found that they are both dominated by tip motion, as can be seen in figure 7(c)–(g) and (m)–(q). In order to quantify the participation of the beam and tip in a specific mode shape, two factors are considered in the freely vibrating case (out-of-contact). The first factor is the value of $\lambda_2 L_2$ compared to the Euler–Bernoulli (E–B) fixed-free eigenvalues. The second factor considered is the ratio between the maximum displacement of the tip relative to the maximum displacement of the beam, each in its own reference frame. The E–B fixed-free eigenvalues are determined from the characteristic equation: $\cos(\beta_n L) \cdot \cosh(\beta_n L) + 1 = 0$, with the first two solutions presented in table 5. $\lambda_2 L_2$ is the separation constant for the tip equation of motion, and is related to the eigenvalues of the system by the relation presented in section 2: $\lambda_2 L_2 = \lambda_1 L_1 \sqrt{R_d}$. The free eigenfrequencies of the entire system, presented in table 5, and equation (17) with the calculated $\tilde{C}$ parameter, are used to calculate the eigenvalues $\lambda_1 L_1$. Then, the relation between the separation constants given above is used, to find $\lambda_2 L_2$. By considering the ratio between $\lambda_2 L_2$ and the fixed-free E–B eigenvalues $\beta_n L$, very high similarity is found. Furthermore, the ratio between the tip maximum displacement and the beam maximum displacement is almost 3 orders of magnitude. The similarity between $\lambda_2 L_2$ and the E–B

Table 5. Investigation of mode A and C behavior. Comparison of the $\lambda_2 L_2$ and the E–B fixed-free eigenvalues, and the ratio between the maximum displacement of the tip and beam in their own reference frames $\frac{\max(W_{2,r})}{\max(W_{1,r})}$ for the rth mode.

	f_n^0 (kHz)	$\lambda_2 L_2$	$\beta_n L$	$\frac{\lambda_2 L_2}{\beta_n L}$	$\frac{\max(W_{2,r})}{\max(W_{1,r})}$
Mode A	65.1	1.8740	1.8751	0.9994	913.4
Mode C	408.3	4.6934	4.6941	0.9999	973.7

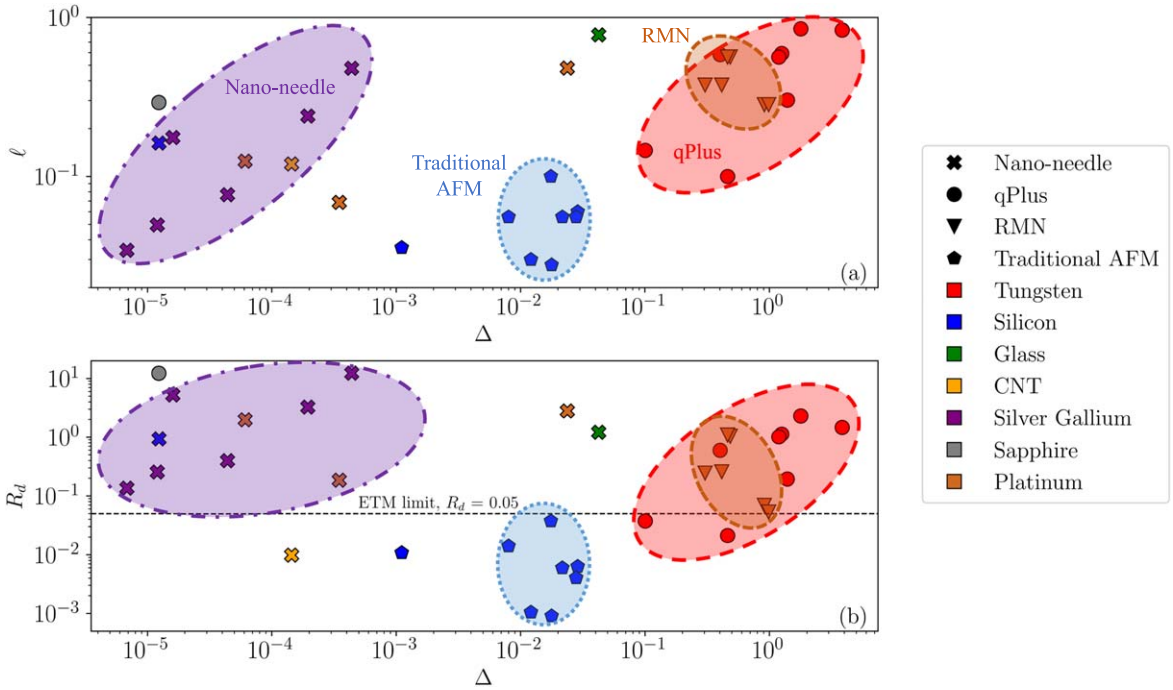

Figure 9. A review of the nondimensional parameters for sensors tips. (a) ℓ as a function of Δ. (b) R_d as a function of Δ.

fixed-free eigenvalues, and the large difference in the tip and beam displacements, determines that modes A and C are by and large tip motion dominant modes, with negligible beam participation. With that in mind, the effect of the normal spring on a tip motion dominated mode is negligible, because the motion at the end of the L-shaped beam is primarily orthogonal to the normal spring direction for tip-motion dominated modes. Therefore, data from two tip modes, such as mode A and C, does not provide sufficient information to solve for both α and ϕ in a multi-modal procedure.

The multi-modal prediction results demonstrate the necessity in identifying the eigenmode interactions for suitable selection of modes and ranges for prediction. Nonetheless, the range in which the eigenmode veering is occurring is found to be mostly unsuitable for prediction using either the single mode or the multi-modal prediction procedures.

4.3. Elastic tip model range

In this section, the physical parameter range in which the use of the ETM is required for prediction accuracy will be examined, as opposed to previously discussed models. First, different tips used for atomic force microscopy are reviewed. The findings are divided into four different groups: Nano-needles, qPlus, Rocky Mountain nanotechnology (RMN), and traditional AFM sensors. The domain of system parameters for these different tip geometries is inspected. Findings are plotted in figure 9. Ellipses are used to circle 4 different groups found in the data, representative of the 4 groups of sensor tips: Nano-needle (purple), qPlus (red), RMN (light brown), and traditional AFM sensors (blue).

For traditional AFM sensors a pyramidal tip of height 12.5 μm is assumed, and a square base of length 11 μm. The static stiffness of a pyramidal tip is estimated using a FE static analysis by applying a unit load and measuring the directional displacement. Once the static displacement of the tip is found, and the nondimensional tip mass is calculated based on the geometry, the definition of $R_d = \sqrt{\frac{k_c}{k_t} \cdot \Delta}$ is used to estimate the level of dynamic coupling between the beam and the tip. The RMN sensors are solid platinum sensors with large conical tips. The static stiffness of the conical tips are estimated using [50]. The traditional AFM sensors combine low Δ, R_d, and ℓvalues, thus validated CR models are widely available and reviewed in [51]. The RMN sensors include significant tip mass and length, and are unlikely to perform well using CR models that do not include these effects in the model. The dynamic coupling parameter R_d for the RMN sensors varies from about $R_d = 0.05$ to approximately $R_d = 1.2$. For such a wide range, a differentiation between the use of the ETM presented here, to the use of the rigid tip model (RTM) presented in [20] is required. Zimron-Politi and Tung [21] have used an RMN sensor in CR and compared the data analysis of using a traditional CR model [2] to the RTM. Their findings showed that no results were obtained for the traditional CR model while the use of the RTM was limited to about 10% error. They have also suggested that elastic effects from the tip affected their results in both the estimation of the system parameters and the CR analysis.

Considering the nano-needles, it is found that in most cases the tip mass is relatively small, even compared to traditional AFM sensors. Nonetheless, in most cases considered for the nano-needles, the dynamic coupling R_d is large. Using the qPlus sensors, a combination of large tip mass and length, along with large dynamic coupling, in some cases are found. The qPlus sensors studied here vary almost three orders of magnitude from approximately $R_d = 0.02$ to $R_d = 12.5$.

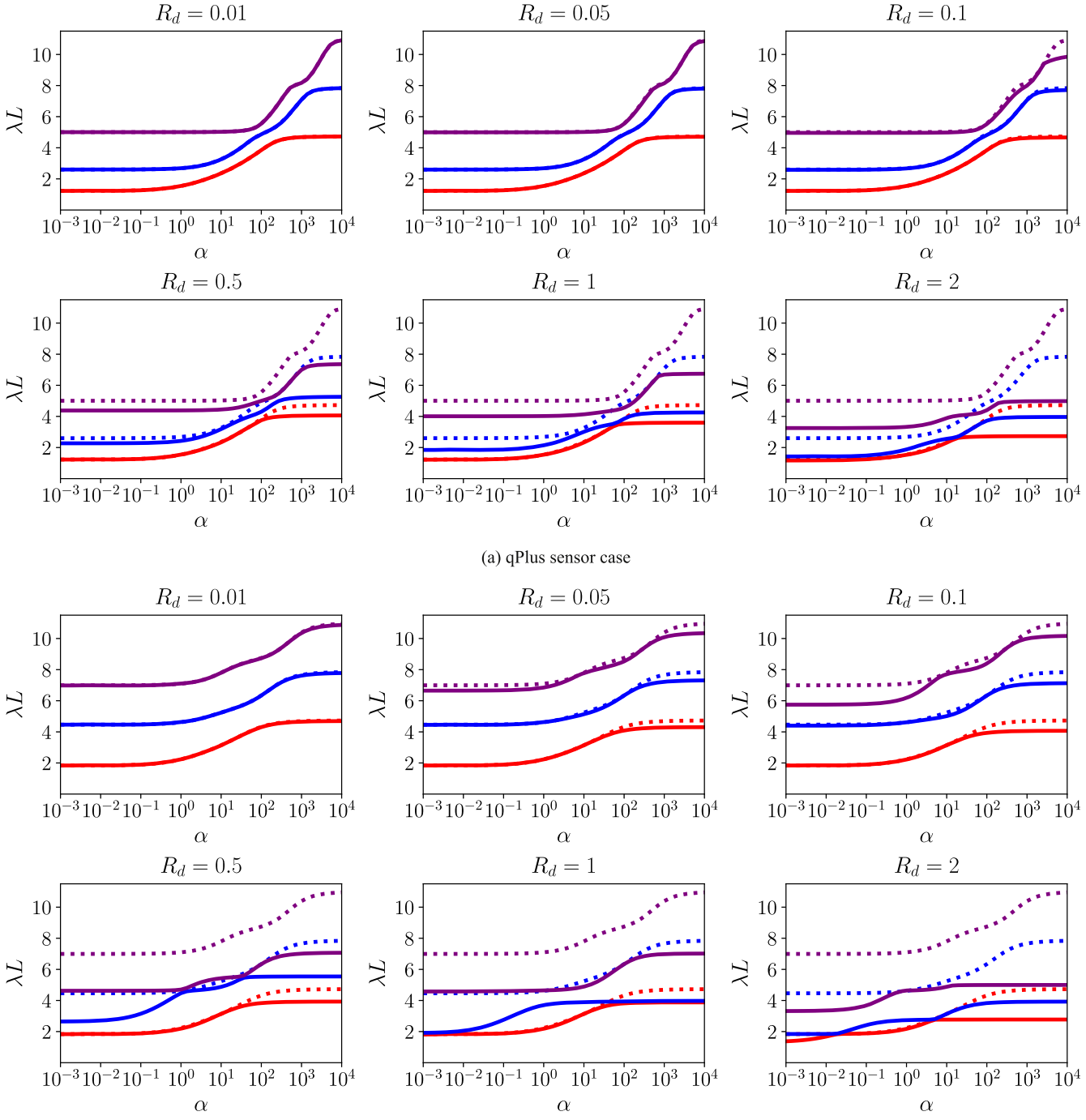

(a) qPlus sensor case

(b) Nano-needle sensor case

Figure 10. The 3 lowest eigenvalues calculated using both ETM (solid lines) and RTM (dotted lines). Each of the figures represent a different R_d case for the ETM results, while the RTM results are unaffected. Mode 1 in red, Mode 2 in blue, and Mode 3 in purple.

To estimate the ranges in which the ETM is recommended for use, it is compared with the RTM, which is considered the closest CR model to the ETM to date. The ETM deviates from the RTM by considering the dynamic effects from the vibrations of the tip, encapsulated in the nondimensional parameter R_d. The first three eigenvalues are calculated using both the ETM and RTM for a range of α values, and for different values of R_d. In figures 10(a) and (b), the comparison between the ETM and RTM results for the cases of qPlus and nano-needle sensors, respectively, is plotted. The values presented in tables 2 and 4 for Δ, $\hat{I}_t$, and ℓ are utilized.

Based on the two cases studied here: a massive tip qPlus sensor and a light tip nano-needle sensor, it is found that the expected deviation between the ETM and RTM begins at R_d values as low as 0.05. Furthermore, it is found that the higher the mode number is, the deviation between the two models begins for a lower α value. For cases in which one of the 3

lowest eigenvalues includes significant tip motion, and cannot be estimated based only by the beam motion, the use of the RTM will become highly inaccurate.

5. Conclusions

In this work, a new theoretical model for the vibrations of an L-shaped beam fixed at one end, and elastically supported at the other end by two linear springs is introduced. A derivation of the characteristic equation for the vibration analysis of the system is presented, along with the eigenvectors. The orthogonality condition for the system is derived and used as a sensitivity function to examine the existence of eigenmode veering and crossing, with the change in the nondimensional sample stiffness. A scheme for the use of out-of-contact experimental data for the calculation of the system's nondimensional parameters is presented and used during a numerical experiment. A numerical experiment is used to mimic contact resonance atomic force microscopy, using long elastic tips for verification of the new model. A finite element modal analysis results of an AFM qPlus sensor, and a microsensor equipped with a nano-needle, is used as the setup of the numerical experiment. The results show that in spite of eigenmode veering in the data, the proposed model is able to predict the sample stiffness with a relative error of no more than 10% for significant practical ranges, using several different modes. The percent of relative error for both numerical experiment cases are presented in figures 5(c) and 8(b), and summarize the verification of the model. Considering the two example cases of a qPlus sensor and a nano-needle discussed in this work, it is found that the use of the ETM is crucial for systems with $R_d > 0.05$.

For cases in which CR multi-modal analysis is performed, to solve for an additional system parameter along with α, the ability to detect and compensate for eigenmode veering and crossing is highly important. For cases where the two modes used for multi-modal analysis are interacting with each other by veering or crossing, no degradation to the prediction is expected. Conversely, if one (or two) of the modes used for multi-modal analysis is interacting with other modes, significant error in the prediction of the variables is expected.

To date, the proposed ETM is the only contact resonance model accounting for tip flexibility. All prior CR models are based on a single beam with various boundary conditions, where the tip flexibility is neglected. The use of a two-beam model to account for both beam and tip motion, opens new venues in CR. Though the discussion mostly focuses on prediction accuracy, note that the ETM is the *only* CR model to predict any tip motion.

The use of long, massive, elastic tips give rise to an increase in the out-of-plane modes. The ETM focuses on the in-plane transverse vibration of the beam-tip-sample system. The AFM user is encouraged to utilize both transverse and lateral channels to properly infer transverse modes. The use of additional sensors, such as a laser Doppler vibrometer, can also assist the experimentalist in the identification of transverse modes.

The model presented in this work is also of interest to the structural dynamics community as it is can be used for the prediction of a L-shaped structure eigenfrequencies and corresponding eigenmodes. An extension to this work may include incorporating sample visco-elasticity, axial flexibility of the structure, adjustable tip location, tilt angle with respect to the sample, and the inclusion of out-of-plane modes in the analytical model.

Acknowledgments

This material is based in part upon work supported by the National Science Foundation under Grant No. 1934772.

Data availability statement

The data that support the findings of this study are available from the corresponding author upon reasonable request.

Appendix A. Elements of matrix M

The elements of matrix M_{ij}, presented in equation (11), are as follows:

Let us use $\lambda_1 L_1 = \lambda L$ for simplicity.

$$M_{1,1} = (\cos(\lambda L) + \cosh(\lambda L))(\lambda L)^2.$$

$$M_{1,2} = (\sinh(\lambda L) + \sin(\lambda L))(\lambda L)^2.$$

$$M_{1,3} = \frac{\ell}{R_d^{\frac{3}{2}}}(\Delta(\lambda L)^3 R_d \cos(\lambda L\sqrt{R_d}) + 3\sin(\lambda L\sqrt{R_d}) R_d^{\frac{3}{2}}\alpha\phi - \sin(\lambda L\sqrt{R_d})\Delta(\lambda L)^2\sqrt{R_d}).$$

$$M_{1,4} = \frac{-3\ell}{R_d^{\frac{3}{2}}}\left(\left(\frac{-\Delta}{3}(\lambda L)^2\sqrt{R_d} - R_d^{\frac{3}{2}}\alpha\phi\right)\cosh(\lambda L\sqrt{R_d}) + \left(R_d^{\frac{3}{2}}\alpha\phi - \frac{1}{3}\Delta(\lambda L)^2\sqrt{R_d}\right)\cos(\lambda L\sqrt{R_d}) - \frac{1}{3}\Delta(\lambda L)^2(\lambda L\, R_d \sin(\lambda L\sqrt{R_d}) - \lambda L\, R_d \sinh(\lambda L\sqrt{R_d}) - 2\sqrt{R_d})).$$

$$M_{1,5} = \frac{\ell}{R_d^{\frac{3}{2}}}(-\Delta(\lambda L)^3 R_d \cosh(\lambda L\sqrt{R_d}) + 3\sinh(\lambda L\sqrt{R_d}) R_d^{\frac{3}{2}}\alpha\phi + \sinh(\lambda L\sqrt{R_d})\Delta(\lambda L)^2\sqrt{R_d}).$$

$$M_{2,1} = (\sinh(\lambda L) - \sin(\lambda L))(\lambda L)^3 - ((\lambda L)^4\Delta - 3\alpha)(\cos(\lambda L) - \cosh(\lambda L)).$$

$$M_{2,2} = (\cos(\lambda L) + \cosh(\lambda L))(\lambda L)^3 - ((\lambda L)^4\Delta - 3\alpha)(-\sinh(\lambda L) + \sin(\lambda L)).$$

$$M_{2,3} = 0.$$
$$M_{2,4} = 0.$$
$$M_{2,5} = 0.$$
$$M_{3,1} = -\ell(\sinh(\lambda L) + \sin(\lambda L)).$$
$$M_{3,2} = \ell(\cos(\lambda L) - \cosh(\lambda L)).$$
$$M_{3,3} = \sqrt{R_d}.$$
$$M_{3,4} = 0.$$
$$M_{3,5} = \sqrt{R_d}.$$
$$M_{4,1} = 0.$$
$$M_{4,2} = 0.$$
$$M_{4,3} = -\sin(\lambda L\sqrt{R_d}).$$
$$M_{4,4} = \cosh(\lambda L\sqrt{R_d}) + \cos(\lambda L\sqrt{R_d}).$$
$$M_{4,5} = \sinh(\lambda L\sqrt{R_d}).$$
$$M_{5,1} = 0.$$
$$M_{5,2} = 0.$$
$$M_{5,3} = -\frac{R_d}{3\,\Delta}(\Delta(\lambda L)^3\sqrt{R_d}\cos(\lambda L\sqrt{R_d}) + 3\sin(\lambda L\sqrt{R_d})R_d\alpha\phi).$$
$$M_{5,4} = \frac{R_d}{\Delta}\left(\frac{\Delta(\lambda L)^3}{3}\sinh(\lambda L\sqrt{R_d})\sqrt{R_d} - \frac{\Delta(\lambda L)^3}{3}\sin(\lambda L\sqrt{R_d})\sqrt{R_d} + \cos(\lambda L\sqrt{R_d})R_d\alpha\phi - \cosh(\lambda L\sqrt{R_d})R_d\alpha\phi\right).$$
$$M_{5,5} = \frac{R_d}{3\,\Delta}(\Delta(\lambda L)^3\cosh(\lambda L\sqrt{R_d})\sqrt{R_d} - 3\sinh(\lambda L\sqrt{R_d})R_d\alpha\phi).$$

Appendix B. Orthogonality condition

Here, the orthogonality condition for the model developed in this work is derived. To begin, consider the nondimensional form of the EOM for the beam, given in equation (5), for two distinct solutions, mode r and mode s:

$$W_{1,r}'''' = (\lambda_{1,r}L_1)^4 \cdot W_{1,r}, \tag{B1}$$
$$W_{1,s}'''' = (\lambda_{1,s}L_1)^4 \cdot W_{1,s}. \tag{B2}$$

where $W_{1,n}$ is the spatial solution to the deflection of the 'beam' section for the nth mode, and $W_{2,n}$ is the spatial solution to the deflection of the 'tip' section for the nth mode. Multiplying equation (B1) by $W_{1,s}$, equation (B2) by $W_{1,r}$, and integrating over the domain gives:

$$\int_0^1 W_{1,r}'''' \cdot W_{1,s} \cdot d\zeta_1 = \int_0^1 (\lambda_{1,r}L_1)^4 \cdot W_{1,r} \cdot W_{1,s} \cdot d\zeta_1, \tag{B3}$$

$$\int_0^1 W_{1,s}'''' \cdot W_{1,r} \cdot d\zeta_1 = \int_0^1 (\lambda_{1,s}L_1)^4 \cdot W_{1,s} \cdot W_{1,r} \cdot d\zeta_1. \tag{B4}$$

Subtracting equations (B4) from (B3) leads to:

$$\int_0^1 (W_{1,r}'''' \cdot W_{1,r} - W_{1,s}'''' \cdot W_{1,r}) \cdot d\zeta_1 = ((\lambda_{1,r}L_1)^4 - (\lambda_{1,s}L_1)^4) \cdot \int_0^1 W_{1,r} \cdot W_{1,s} \cdot d\zeta_1. \tag{B5}$$

Applying integration by parts twice to the left hand side of equation (B5), and using the boundary conditions given in equation (9) gives:

$$((\lambda_{1,r}L_1)^4 - (\lambda_{1,s}L_1)^4) \cdot \left\{\int_0^1 W_{1,r} \cdot W_{1,s} \cdot d\zeta_1 + W_{1,r}(1) \cdot \Delta \cdot W_{1,s}(1) + W_{1,r}'(1) \cdot \hat{I}_t \cdot W_{1,s}'(1)\right\} + \Delta\ell^2 \cdot \int_0^1 \zeta_2 \cdot ((\lambda_{1,r}L_1)^4 \cdot W_{2,r} \cdot W_{1,s}'(1) - (\lambda_{1,s}L_1)^4 \cdot W_{2,s} \cdot W_{1,r}'(1)) \cdot d\zeta_2 = 3\alpha\phi\ell^2 \cdot (W_{1,s}'(1) \cdot W_{2,r}(1) - W_{1,r}'(1) \cdot W_{2,s}(1)). \tag{B6}$$

Next, consider the nondimensional form of the EOM for the tip, given in equation (6), for two distinct solutions, mode r and mode s:

$$W_{2,r}'''' = (\lambda_{2,r}L_2)^4 \cdot (W_{2,r} + \zeta_2 \cdot W_{1,r}'(1)), \tag{B7}$$
$$W_{2,s}'''' = (\lambda_{2,s}L_2)^4 \cdot (W_{2,s} + \zeta_2 \cdot W_{1,s}'(1)). \tag{B8}$$

Multiplying equation (B7) by $W_{2,s}$, and equation (B8) by $W_{2,r}$ and integrating over the domain gives:

$$\int_0^1 W_{2,r}'''' \cdot W_{2,s} \cdot d\zeta_2 = \int_0^1 (\lambda_{2,r}L_2)^4 \cdot (W_{2,r} + \zeta_2 \cdot W_{1,r}'(1)) \cdot W_{2,s} \cdot d\zeta_2, \tag{B9}$$

$$\int_0^1 W_{2,s}'''' \cdot W_{2,r} \cdot d\zeta_2 = \int_0^1 (\lambda_{2,s}L_2)^4 \cdot (W_{2,s} + \zeta_2 \cdot W_{1,s}'(1)) \cdot W_{2,r} \cdot d\zeta_2. \tag{B10}$$

Subtracting equations (B10) from (B9) leads to:

$$\int_0^1 (W_{2,r}'''' \cdot W_{2,s} - W_{2,s}'''' \cdot W_{2,r}) \cdot d\zeta_2 = ((\lambda_{2,r}L_2)^4 - (\lambda_{2,s}L_2)^4) \cdot \int_0^1 W_{2,r} \cdot W_{2,s} \cdot d\zeta_2 + (\lambda_{2,r}L_2)^4 \cdot \int_0^1 \zeta_2 \cdot W_{2,s} \cdot W_{1,r}'(1) \cdot d\zeta_2 - (\lambda_{2,s}L_2)^4 \cdot \int_0^1 \zeta_2 \cdot W_{2,r} \cdot W_{1,s}'(1) \cdot d\zeta_2. \tag{B11}$$

Applying integration by parts twice to the left hand side of equation (B11), and using the boundary conditions given in equation (9) gives:

$$R_d^2 \cdot ((\lambda_{1,r}L_1)^4 - (\lambda_{1,s}L_1)^4) \cdot \int_0^1 W_{2,r} \cdot W_{2,s} \cdot d\zeta_2 + R_d^2 \cdot \int_0^1 \zeta_2 \cdot ((\lambda_{1,r}L_1)^4 \cdot W_{2,s} \cdot W_{1,r}'(1) - (\lambda_{1,s}L_1)^4 \cdot W_{2,r} \cdot W_{1,s}'(1)) \cdot d\zeta_2 = 3\alpha\phi\frac{R_d^2}{\Delta} \cdot (W_{2,s}(1) \cdot W_{1,r}'(1) - W_{2,r}(1) \cdot W_{1,s}'(1)). \tag{B12}$$

Multiplying equation (B12) by $\frac{\Delta \cdot \ell^2}{R_d^2}$ and subtracting it from equation (B6) gives:

$$((\lambda_{1,r}L_1)^4 - (\lambda_{1,s}L_1)^4) \cdot \left\{ \int_0^1 W_{1,r} \cdot W_{1,s} \cdot d\zeta_1 + W_{1,r}(1) \cdot \Delta \cdot W_{1,s}(1) + W'_{1,r}(1) \cdot \hat{I}_t \cdot W_{1,s}{}'(1) + \Delta\ell^2 \cdot \int_0^1 [W_{2,r} \cdot W_{2,s} + \zeta_2 \cdot (W_{2,r} \cdot W_{1,s}{}'(1) + W_{2,s} \cdot W'_{1,r}(1))] \cdot d\zeta_2 \right\} = 0. \tag{B13}$$

Recalling that r and s are distinct modes ($\lambda_{1,r}L_1 \neq \lambda_{1,s}L_1$), the orthogonality condition is obtained:

$$\int_0^1 W_{1,r} \cdot W_{1,s} \cdot d\zeta_1 + W_{1,r}(1) \cdot \Delta \cdot W_{1,s}(1) + W'_{1,r}(1) \cdot \hat{I}_t \cdot W_{1,s}{}'(1) + \Delta\ell^2 \cdot \int_0^1 [W_{2,r} \cdot W_{2,s} + \zeta_2 \cdot (W_{2,r} \cdot W_{1,s}{}'(1) + W_{2,s} \cdot W'_{1,r}(1))] \cdot d\zeta_2 = 0. \tag{B14}$$

The first row of equation (B14) represents the beam section with the end mass and rotational inertia and is identical to the result obtained in [52]. The second row represents the effects from the elastic tip section and the overall orthogonality condition obtained here is equivalent to the one given in [34] for the case of an 'L-shaped' beam with no additional mass. As expected, the effects from the springs discussed in this work (and not discussed in [34] cancel out, and do not affect the final result [38]. Following the orthogonality condition obtained in equation (B14), define:

$$\int_0^1 W_{1,r} \cdot W_{1,s} \cdot d\zeta_1 + W_{1,r}(1) \cdot \Delta \cdot W_{1,s}(1) + W'_{1,r}(1) \cdot \hat{I}_t \cdot W_{1,s}{}'(1) + \Delta\ell^2 \cdot \int_0^1 [W_{2,r} \cdot W_{2,s} + \zeta_2 \cdot (W_{2,r} \cdot W_{1,s}{}'(1) + W_{2,s} \cdot W'_{1,r}(1))] \cdot d\zeta_2 = \delta_{rs}. \tag{B15}$$

ORCID iDs

Nadav Zimron-Politi https://orcid.org/0000-0001-6141-3560
Ryan C Tung https://orcid.org/0000-0003-2862-6980

References

[1] Rabe U and Arnold W 1994 Acoustic microscopy by atomic force microscopy *Appl. Phys. Lett.* **64** 1493–5
[2] Rabe U, Janser K and Arnold W 1996 Vibrations of free and surface-coupled atomic force microscope cantilevers: theory and experiment *Rev. Sci. Instrum.* **67** 3281–93
[3] Ding X, Kuang B, Xiong C, Mao R, Xu Y, Wang Z and Hu H 2022 A super high aspect ratio atomic force microscopy probe for accurate topography and surface tension measurement *Sensors Actuators*A **347** 113891
[4] Efremov Y M, Suter D M, Timashev P S and Raman A 2022 3d nanomechanical mapping of subcellular and sub-nuclear structures of living cells by multi-harmonic afm with long-tip microcantilevers *Sci. Rep.* **12** 529
[5] Jafari A and Sadeghi A 2023 A new insight into the mechanical properties of nanobiofibers and vibrational behavior of atomic force microscope beam considering them as the samples *J. Mech. Behav. Biomed. Mater.* **142** 105842
[6] Sajjadi M, Chahari M, Pishkenari H N and Vossoughi G 2022 Designing nonlinear observer for topography estimation in trolling mode atomic force microscopy *J. Vib. Control* **28** 3890–905
[7] Guan D, Barraud C, Charlaix E and Tong P 2017 Noncontact viscoelastic measurement of polymer thin films in a liquid medium using long-needle atomic force microscopy *Langmuir* **33** 1385–90
[8] Minary-Jolandan M, Tajik A, Wang N and Yu M-F 2012 Intrinsically high-q dynamic afm imaging in liquid with a significantly extended needle tip *Nanotechnology* **23** 235704
[9] Mohammadi S Z, Moghadam M and Pishkenari H N 2019 Dynamical modeling of manipulation process in trolling-mode afm *Ultramicroscopy* **197** 83–94
[10] Shibata M, Uchihashi T, Ando T and Yasuda R 2015 Long-tip high-speed atomic force microscopy for nanometer-scale imaging in live cells *Sci. Rep.* **5** 8724
[11] Tung R C, Jana A and Raman A 2008 Hydrodynamic loading of microcantilevers oscillating near rigid walls *J. Appl. Phys.* **104** 114905
[12] Tung R C, Killgore J P and Hurley D C 2014 Liquid contact resonance atomic force microscopy via experimental reconstruction of the hydrodynamic function *J. Appl. Phys.* **115** 224904
[13] Aureli M and Porfiri M 2010 Low frequency and large amplitude oscillations of cantilevers in viscous fluids *Appl. Phys. Lett.* **96** 164102
[14] Sader J E 1998 Frequency response of cantilever beams immersed in viscous fluids with applications to the atomic force microscope *J. Appl. Phys.* **84** 64–76
[15] Green C P and Sader J E 2005 Small amplitude oscillations of a thin beam immersed in a viscous fluid near a solid surface *Phys. Fluids* **17** 073102
[16] Giessibl F J 1998 High-speed force sensor for force microscopy and profilometry utilizing a quartz tuning fork *Appl. Phys. Lett.* **73** 3956–8
[17] Giessibl F J 2019 The qplus sensor, a powerful core for the atomic force microscope *Rev. Sci. Instrum.* **90** 011101
[18] Gross L, Mohn F, Moll N, Liljeroth P and Meyer G 2009 The chemical structure of a molecule resolved by atomic force microscopy *Science* **325** 1110–4
[19] Chen P, Fan D, Selloni A, Carter E A, Arnold C B, Zhang Y, Gross A S, Chelikowsky J R and Yao N 2023 Observation of electron orbital signatures of single atoms within metal-phthalocyanines using atomic force microscopy *Nat. Commun.* **14** 1460
[20] Jaquez-Moreno T, Aureli M and Tung R C 2019 Contact resonance atomic force microscopy using long, massive tips *Sensors* **19** 4990
[21] Zimron-Politi N and Tung R C 2023 Experimental validation of contact resonance afm using long massive tips *Nanotechnology* **34** 365712
[22] Solares S D and Cartagena-Rivera A X 2022 Frequency-dependent nanomechanical profiling for medical diagnosis *Beilstein J. Nanotechnol.* **13** 1483–9

[23] Stylianou A, Kontomaris S-V, Grant C and Alexandratou E 2019 Atomic force microscopy on biological materials related to pathological conditions *Scanning* **2019** 8452851
[24] Lyonnais S, Hénaut M, Neyret A, Merida P, Cazevieille C, Gros N, Chable-Bessia C and Muriaux D 2021 Atomic force microscopy analysis of native infectious and inactivated sars-cov-2 virions *Sci. Rep.* **11** 11885
[25] Han S W, Nakamura C, Obataya I, Nakamura N and Miyake J 2005 A molecular delivery system by using afm and nanoneedle *Biosens. Bioelectron.* **20** 2120–5
[26] Han S-W, Nakamura C, Kotobuki N, Obataya I, Ohgushi H, Nagamune T and Miyake J 2008 High-efficiency dna injection into a single human mesenchymal stem cell using a nanoneedle and atomic force microscopy, Nanomedicine: Nanotechnology *Biol. Med.* **4** 215–25
[27] Gopal S, Chiappini C, Penders J, Leonardo V, Seong H, Rothery S, Korchev Y, Shevchuk A and Stevens M M 2019 Porous silicon nanoneedles modulate endocytosis to deliver biological payloads *Adv. Mater.* **31** 1806788
[28] Amiri Moghadam A A, Torabi K, Moavenian M and Davoodi R 2013 Dynamic modeling and robust control of an l-shaped microrobot based on fast trilayer polypyrrole-bending actuators *J. Intell. Mater. Syst. Struct.* **24** 484–98
[29] Iseki T, Okumura M, Sugawara T and Kurosawa M K 2012 Deflection properties of a mems optical scanner with four torsion beams and l-shaped arms *Sensors Actuators*A **178** 154–63
[30] Shi S, Geng W, Bi K, Shi Y, Li F, He J and Chou X 2022 High sensitivity mems accelerometer using pzt-based four l-shaped beam structure *IEEE Sensors J.* **22** 7627–36
[31] Erturk A, Renno J M and Inman D J 2009 Modeling of piezoelectric energy harvesting from an l-shaped beam-mass structure with an application to uavs *J. Intell. Mater. Syst. Struct.* **20** 529–44
[32] Liu D, Al-Haik M, Zakaria M and Hajj M R 2018 Piezoelectric energy harvesting using l-shaped structures *J. Intell. Mater. Syst. Struct.* **29** 1206–15
[33] Li H, Liu D, Wang J, Shang X and Hajj M R 2020 Broadband bimorph piezoelectric energy harvesting by exploiting bending-torsion of l-shaped structure *Energy Convers. Manage.* **206** 112503
[34] Oguamanam D, Hansen J and Heppler G 1998 Vibration of arbitrarily oriented two-member open frames with tip mass *J. Sound Vib.* **209** 651–69
[35] Bang H 1996 Analytical solution for dynamic analysis of a flexible l-shaped structure *J. Guid. Control Dyn.* **19** 248–50
[36] Heppler G, Oguamanam D and Hansen J 2003 Vibration of a two-member open frame *J. Sound Vib.* **263** 299–317
[37] He K and Zhu W 2011 Finite element modeling of structures with l-shaped beams and bolted joints *J. Vib. Acoust.* **133** 011011
[38] Meirovitch L 1967 *Analytical Methods in Vibrations* (MacMillan)
[39] Kreyszig E 2010 *Advanced Engineering Mathematics* (Wiley) 10th edn
[40] Huang J, Krousgrill C M and Bajaj A K 2006 Modeling of automotive drum brakes for squeal and parameter sensitivity analysis *J. Sound Vib.* **289** 245–63
[41] Rabe U, Amelio S, Kester E, Scherer V, Hirsekorn S and Arnold W 2000 Quantitative determination of contact stiffness using atomic force acoustic microscopy *Ultrasonics* **38** 430–7
[42] Mazeran P-E and Loubet J-L 1999 Normal and lateral modulation with a scanning force microscope, an analysis: implication in quantitative elastic and friction imaging *Tribol. Lett.* **7** 199–212
[43] Ma C, Zhou C, Peng J, Chen Y, Arnold W and Chu J 2021 Thermal noise in contact atomic force microscopy *J. Appl. Phys.* **129** 234303
[44] Yamada Y, Ichii T, Utsunomiya T, Kimura K, Kobayashi K, Yamada H and Sugimura H 2023 Fundamental and higher eigenmodes of qplus sensors with a long probe for vertical-lateral bimodal atomic force microscopy *Nanoscale Adv.* **5** 840–50
[45] Espinoza-Beltrán F, Geng K, Saldaña J M, Rabe U, Hirsekorn S and Arnold W 2009 Simulation of vibrational resonances of stiff afm cantilevers by finite element methods *New J. Phys.* **11** 083034
[46] Dobrokhotov V V, Yazdanpanah M M, Pabba S, Safir A and Cohn R W 2007 Visual force sensing with flexible nanowire buckling springs *Nanotechnology* **19** 035502
[47] Giessibl F J and Reichling M 2005 Investigating atomic details of the CaF_2 (111) surface with a qplus sensor *Nanotechnology* **16** S118
[48] Johnson K L and Johnson K L 1987 *Contact Mechanics* (Cambridge University Press)
[49] Hurley D C 2009 Contact resonance force microscopy techniques for nanomechanical measurements *Applied Scanning Probe Methods XI* (Springer) pp 97–138
[50] McCutcheon W J 1983 Deflections and stresses in circular tapered beams and poles *Civil Engineering for Practicing and Design Engineers* **2** 207–33
[51] Rabe U 2006 Atomic force acoustic microscopy *Applied Scanning Probe Methods II: Scanning Probe Microscopy Techniques* (Springer) pp 37–90
[52] Erturk A and Inman D 2011 Appendix C: modal analysis of a uniform cantilever with a tip mass *Piezoelectric Energy Harvesting* 353–66